

# Correct-by-Construction Vision-based Pose Estimation using Geometric Generative Models

Ulices Santa Cruz\*, Mahmoud Elfar\*, and Yasser Shoukry\*

**Abstract**—In this paper, we consider the problem of vision-based pose estimation for autonomous systems. While deep neural networks have been successfully used for vision-based tasks, they inherently lack provable guarantees on the correctness of their output, which is crucial for safety-critical applications. This paper presents a framework for designing certifiable neural networks (NNs) for perception-based pose estimation that integrates physics-driven modeling with learning-based estimation. The proposed framework begins by leveraging the known geometry of planar objects commonly found in the environment, such as traffic signs and runway markings, referred to as target objects. At its core, it introduces a geometric generative model (GGM), a neural-network-like model whose parameters are derived from the image formation process of a target object observed by a camera. Once designed, the GGM can be used to train NN-based pose estimators with certified guarantees in terms of their estimation errors. Thanks to the GGM, these certified guarantees hold even for data that were not present during the training of these NN-estimators. We first demonstrate this framework in uncluttered environments, where the target object is the only object present in the camera’s field of view. To generalize the framework to more realistic scenarios, we next show how the employ ideas from NN reachability analysis to design certified object NN that can detect the presence of the target object in cluttered environments. Subsequently, the framework consolidates the certified object detector with the certified pose estimator to design a multi-stage perception pipeline that generalizes the proposed approach to cluttered environments, while maintaining its certified guarantees. We evaluate the proposed framework using both synthetic and real images of various planar objects commonly encountered by autonomous vehicles. Using images captured by an event-based camera, we show that the trained encoder can effectively estimate the pose of a traffic sign in accordance with the certified bound provided by the framework.

**Index Terms**—Formal Verification, Reachability Analysis, Pose Estimation, Vision-Based Perception, Certifiable Neural Networks, Safety-Critical Systems

## I. INTRODUCTION

Autonomous vehicles rely on a variety of sensors to estimate their pose and perceive nearby objects in order to safely navigate their environment. Imaging sensors are particularly vital for detecting and recognizing objects of interest, such as road marks, traffic signs, lane dividers and runway markings. In recent years, deep Neural Networks (NNs) have been successfully deployed in autonomous vehicles to process images captured by cameras and provide high-level semantic information about the environment that contributes to the vehicle’s perception of its surroundings and the objects within

The authors are with the Department of Electrical Engineering and Computer Science, University of California, Irvine, CA 92697, USA. Email: {usantacr, elfarm, yshoukry}@uci.edu

them. deep NNs outperform traditional computer vision algorithms in tasks such as object detection, recognition and tracking, becoming the most prevalent choice for vision-based perception in autonomous vehicles.

However, deep NNs are inherently black-boxes, and thus do not provide guarantees on the correctness of their output. This is particularly problematic for autonomous vehicles where DNNs are used in safety-critical subsystems. For example, a NN-based sign recognition subsystem may misclassify a stop sign, which can lead to loss of life and property. Similarly, an aircraft approaching a runway for landing may rely on a DNN to interpret threshold stripes or centerline markings. An undetected misclassification in this safety-critical stage can lead to significant deviations in the estimated approach trajectory, endangering both passengers and surrounding operations. These examples underscore the central challenge: while end-to-end neural networks excel in perception accuracy under nominal conditions, their lack of certified guarantees leaves safety-critical systems vulnerable to catastrophic errors.

In this paper, we consider the problem of perception-based pose estimation for autonomous vehicles. We focus on environments that contain unique, planar landmarks whose geometry is known a priori. Such landmarks are ubiquitous: traffic signs, road markings, and lane dividers for ground vehicles; or navigation aids [1], runway markings [2], and helipads for aerial vehicles (see Fig. 1). We refer to these landmarks as *target objects*. Given a target object of known planar geometry, the objective is to estimate the position and orientation of an imaging sensor — referred to as the *camera* — relative to the target, using only the images captured by the camera. For instance, a front-facing camera on a autonomous car approaching an intersection may simultaneously observe a stop sign on the roadside and a pedestrian crossing marked on the pavement. Likewise, as shown in Fig. 2, a forward-facing camera on an aircraft descending toward a runway may capture threshold stripes, centerlines, and touchdown zone designators, all of which are planar objects with known geometry. In both cases, the known geometry of the observed target objects enables precise pose estimation, which is crucial for safe navigation and control of the vehicle and its environment.

In this paper, we propose a framework for designing correct-by-construction and certifiable NNs for perception-based pose estimation that comprises three main components. The first component leverages the known geometry of planar target objects to design a NN-like model, referred to as a *geometric generative model* (GGM), that emulates the image formation process of a camera sensor. Specifically, the framework derives the GGM’s architecture and parameters based on the physical

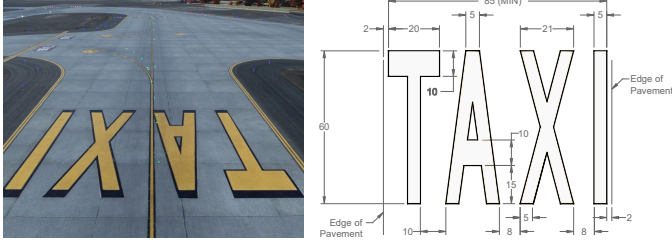


Fig. 1. Example of (left) a taxiway planar marking, and (right) its known geometry (source: [2]) that can be used for vision-based pose estimation.



Fig. 2. Sequence of camera images of an aircraft approaching a runway for autonomously landing. The known geometry of the planar runway markings can be used for vision-based pose estimation.

parameters of the camera and the geometry of the target object. Once designed, a GGM, generates an image of the target object from the perspective of a given camera pose.

The second component provides a systematic approach to train a NN estimator that can estimate the pose of the target object from an image while providing worst case guarantees on the performance of this estimator. Uniquely to our analysis, and thanks to the GGM's NN-like structure, we provide guarantees on the estimation error that generalizes to data that was not present during the NN training.

While the second component addresses the pose estimation problem under ideal conditions in uncluttered environments, the third component extends the framework to more realistic scenarios where multiple objects may be present in the scene. To this end, the framework first tackles the problem of object detection by using light-weight forward reachability algorithm, thanks to the GGM NN like architecture. Once detection is established, the framework consolidates the certified pose estimator with the object detector into a multi-stage perception pipeline that incorporates spatial filtering and reachability-based reasoning. This pipeline enables the framework to generalize certifiable pose estimation to cluttered environments, ensuring reliable operation even in the presence of distractor objects and noise.

We evaluate the proposed framework using both synthetic and real images of various planar objects commonly encountered by autonomous vehicles. In particular, using images captured by an event-based camera, we demonstrate that a trained encoder can effectively estimate the pose of a traffic

sign in accordance with the certified error bounds established by the framework. These results confirm that the proposed framework not only provides formal guarantees in theory but also achieves reliable performance in practice.

In summary, the main contributions of this paper are as follows:

- We design GGMs that capture the image formation process of planar objects based on known geometry and camera parameters.
- We develop a framework for training certifiable NN-based pose estimators that are guaranteed to maintain their certified performance even for data not seen during training.
- We design a multi-stage perception pipeline that uses forward reachability analysis to build certified object detection, when combined with certified pose estimation, enables operation in cluttered environments.
- We demonstrate the effectiveness of the framework through numerical simulations and experiments with event-based camera data.

The rest of this paper is organized as follows. Section II presents the preliminaries on the image formation process of objects from a camera sensor perspective and the abstraction of objects of interest as polytopic complexes, followed by the formulation of the vision-based pose estimation problem. Section III presents the proposed process for designing a GGM that emulates the image formation process of a camera sensor. In Section IV, we introduce the use of the GGM to provide certified bounds for NN-based pose estimators in uncluttered environments. In Section V, we show how to design vision-based object detectors that reason about the presence of a target object in an image. In Section VI, we extend the framework with a multi-stage perception pipeline that integrates detection, spatial filtering, and pose estimation to handle cluttered environments. For evaluation, Section VII describes numerical and experimental results using both synthetic images and real images captured by an event-based camera, demonstrating that the framework achieves reliable and certifiable pose estimation for planar objects commonly encountered by autonomous vehicles.

### Related Work

DNN-based perception and navigation methods have achieved remarkable performance in recent years, particularly in vision-based navigation and pose estimation tasks. End-to-end learning approaches have demonstrated empirical success in tasks such as object detection, semantic segmentation, and pose regression. However, their black-box attributes and lack of provable guarantees on the correctness or robustness of their outputs renders them an unacceptable choice for safety-critical applications. In those applications, such as autonomous driving and aircraft landing, an erroneous perception or an undetected misclassification can propagate downstream and lead to unsafe states where loss of life and property may occur.

To mitigate those challenges, early formal verification methods cast the verification of feedforward NNs as a Satisfiability-Modulo-Theory (SMT) problem [3]. These approaches enable

exhaustive reasoning about the invariance of classification outputs under bounded input perturbations, formally guaranteeing robustness to small image manipulations. While precise, SMT-based methods are computationally expensive and scale poorly with network size or input dimensionality, motivating the development of relaxed reachability and convex-optimization formulations [4]–[7]. Collectively, these methods provide deterministic safety proofs for limited architectures but remain constrained by computational cost and the complexity of image-based inputs.

Standard NN verification techniques struggle with high-dimensional image inputs, motivating specialized approaches for vision-based control systems. One direction uses generative models as camera surrogates, training GANs to map system states to plausible images and enabling reachability analysis on the lower-dimensional combined generator-controller network [8]–[10]. Alternatively, geometric abstraction methods partition 3D scenes into image-invariant regions or construct interval image representations [11]–[15]. While these approaches successfully verify vision-based controllers in specific scenarios, they treat perception model construction and controller design as separate processes, leaving a gap between the perception representation and the downstream control requirements.

Beyond exact verification, several works have sought statistical or contract-based assurance of learned perception systems. Perception-contract frameworks formalize testable specifications for machine learning components using conformal prediction, systematic abstraction, or counterexample-guided synthesis [16]–[22]. Although these methods improve empirical reliability, their guarantees are probabilistic and non-compositional [23]. Control-theoretic approaches instead synthesize controllers provably safe despite bounded perception errors by extending control barrier functions to account for measurement uncertainty [24]–[27]. While effective for runtime safety, these methods assume bounded perception error rather than deriving such bounds from first principles. Meanwhile, advances in vision architectures have pushed the frontier of perception performance [28], but these models remain purely data-driven and unverifiable.

In contrast, our framework unifies physics-based image formation and learning-based estimation within a single certifiable structure. By encoding camera and object geometry through a GGM with network parameters realized through coordinate transformations rather than learned from data, the perception process itself becomes analyzable via reachability methods. This enables certified error bounds on pose estimation—providing a formal layer of correctness absent from existing NN-based perception pipelines.

## II. PRELIMINARIES AND PROBLEM FORMULATION

### A. Notation

We use  $\mathbb{R}$ ,  $\mathbb{N}$ ,  $\mathbb{Z}$  and  $\mathbb{B}$  to denote the set of real, natural, integer and Boolean numbers, respectively. We use  $v_i$  to denote the  $i$ -th component of a vector  $v \in \mathbb{R}^n$ . We also use  $\|v\|_p$  to denote its  $p$ -norm. We use  $M_{ij}$  to denote the  $(i, j)$ -th entry of a matrix  $M \in \mathbb{R}^{m \times n}$ . For a function  $f$ , we use  $\text{dom}(f)$

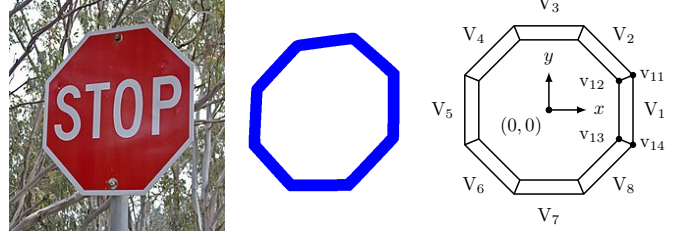


Fig. 3. Example of (left) a stop sign as a target; (center) its image generated by the camera; and (right) its target model composed of 8 polygons representing a non-convex shape.

to denote its domain. We use  $A \vee B$  to denote the element-wise logical OR operation between two matrices  $A$  and  $B$ , and  $A \odot B$  to denote the element-wise (Hadamard) product between them. We use  $\text{Conv}(S)$  to denote the convex hull of a set  $S$ , and  $\mathcal{P}(S)$  to denote its power set. For an angle  $\theta$ , we use the nomenclature  $c_\theta$  and  $s_\theta$  to denote  $\cos(\theta)$  and  $\sin(\theta)$ , respectively. Given a function  $f : \mathcal{X} \rightarrow \mathcal{Y}$  and a set  $S \subseteq \mathcal{X}$ , we use  $\mathcal{R}(f, S)$  to denote the forward reachable set:

$$\mathcal{R}(f, S) = \{y \in \mathcal{Y} \mid \exists x \in S. y = f(x)\}.$$

### B. Target Model

In this work, a *target* is a planar object whose geometry is known a priori, and can be represented by the union of a finite number of convex polygons that lie in the same 2D plane.

**Definition 1** (Target Model). *Given a stationary target in the Euclidean space, the target model is composed of a finite set of convex polygons:*

$$\mathcal{T} = \left\{ V_i \mid i = 1, \dots, N, V_i = (v_{ij})_{j=1}^{n_i}, v_{ij} \in \mathbb{R}^3 \right\},$$

where

- $N$  is the number of convex polygons in the target;
- $V_i$  is the  $i$ -th polygon of size  $n_i$ , defined as a tuple of the polygon's vertices arranged in a CCW winding order;
- $n_i$  is the number of vertices in the  $i$ -th polygon; and
- $v_{ij} = (v_{xij}, v_{yij}, 0)$ ,  $\forall v_{ij} \in V_i$ .

Note that the definition dictates that the polygons are convex and lie in the same 2D plane ( $z = 0$ ), but the target itself does not have to be convex. Also, all vertices are defined with respect to a local coordinate frame attached to the target. We will use  $\bar{\mathcal{T}}$  to denote the set of all objects in the environment other than the target, referred to as the *clutter*. Since the target is stationary, we can use the target coordinate frame as a global reference frame.

**Example 1.** Fig. 3 shows an example of a stop sign as a target. The stop sign is composed of 8 convex polygons, i.e.,  $N = 8$ , together forming a non-convex shape  $\mathcal{T} = \{V_1, \dots, V_8\}$ . Each polygon  $V_i \in \mathcal{T}$  is defined by its vertices, arranged in a counter-clockwise order; e.g.,  $V_1 = (v_{11}, v_{12}, v_{13}, v_{14})$ . While each polygon is convex, the combination of all polygons is a non-convex shape.

### C. Camera Model

In this work, we consider a mobile, monochromatic camera that produces digital images. A camera  $\mathcal{C}$  is characterized by both its intrinsic and extrinsic parameters. The camera's *intrinsic parameters* include its focal length, image sensor resolution, and geometric center (principal point). For simplicity, we assume that the focal length of the camera lens in both the horizontal and vertical directions is the same, denoted by  $f \in \mathbb{R}_{>0}$ . The image sensor resolution is defined by the number of pixel rows (height) and columns (width) of the image, denoted by  $h \in \mathbb{N}$  and  $w \in \mathbb{N}$ , respectively. We will also assume that the principal point of the camera, where the camera's optical axis intersects the image sensor plane, is at the center of the image, that is,  $w/2$  and  $h/2$  in the horizontal and vertical directions, respectively.

The camera's *extrinsic parameters* include its position and orientation, i.e., its *pose*, and are captured by the tuple  $\xi = (x, y, z, \phi, \theta, \psi)$ ,  $\xi \in \Xi \subset \mathbb{R}^6$ , where  $x, y, z$  denote the camera's position with respect to the global coordinate frame;  $\phi, \theta, \psi$  denote its roll, pitch, and yaw angles, respectively; and  $\Xi$  is the pose space. The digital image produced by the camera is denoted by  $I \in \mathbb{B}^{h \times w}$ . We will use  $I(i, j)$  and  $I_{ij}$  to denote the pixel value at the  $i$ -th row and  $j$ -th column of the image. In ideal cases, this image depends only on the target  $\mathcal{T}$ , the camera pose  $\xi$ , as well as the intrinsic parameters of the camera as captured by the following definition.

**Definition 2** (Ideal Camera Model). *Let  $\mathcal{T}$  be a stationary target. The ideal camera model with respect to  $\mathcal{T}$  is a function:*

$$\mathcal{C}_{\mathcal{T}}: \Xi \rightarrow \mathbb{B}^{h \times w} \text{ given by } \mathcal{C}_{\mathcal{T}}(\xi) = I_{\mathcal{T}\xi},$$

where  $\xi \in \Xi$  is the camera pose, and  $I_{\mathcal{T}\xi}$  is the ideal image of the target  $\mathcal{T}$  as observed by the camera at pose  $\xi$ .

In practice, camera models are not ideal, since the image captured by the camera also contains other objects in the scene. Thus, we identify two types of images based on the presence of other objects in the environment, specifically cluttered and uncluttered images.

**Definition 3** (Image Clutter). *Let  $\mathcal{T}$  be a target object. Clutter is defined as the set of all objects in the environment other than the target, denoted by  $\bar{\mathcal{T}}$ . The image  $I(\xi)$ , captured by the camera at pose  $\xi$  in that environment, can be represented as:*

$$I(\xi) = I_{\mathcal{T}\xi} \vee I_{\bar{\mathcal{T}}\xi},$$

where

- $I_{\mathcal{T}\xi}$  is the ideal image of the target, and
- $I_{\bar{\mathcal{T}}\xi}$  is the image of clutter.

We call an environment cluttered if  $\bar{\mathcal{T}} \neq \emptyset$ , i.e., other objects are present in the image, and we call the corresponding image cluttered. Similarly, we call an environment uncluttered if  $\bar{\mathcal{T}} = \emptyset$ , i.e., no other objects are present in the image, and we characterize the corresponding image uncluttered.

This definition is centered around partitioning the objects in the environment into the target object, whose geometry is known a priori, and clutter, whose geometry is unknown.

Based on this partitioning, we can define a system model that captures the target, clutter, camera, and pose space.

**Definition 4** (System Model). *A system model is a tuple  $(\mathcal{T}, \bar{\mathcal{T}}, \mathcal{C}, \Xi)$ , where*

- $\mathcal{T}$  is the target object;
- $\bar{\mathcal{T}}$  is the clutter in the environment;
- $\mathcal{C}: \Xi \rightarrow \mathbb{B}^{h \times w}$ ,  $\xi \mapsto I(\xi)$  is the camera model; and
- $\Xi$  is the pose space of the camera.

Note that the camera model  $\mathcal{C}$  depends on both the target  $\mathcal{T}$  and the clutter  $\bar{\mathcal{T}}$ . In an uncluttered environment (i.e.,  $\bar{\mathcal{T}} = \emptyset$ ), the camera model reduces to the ideal camera model of the target, i.e.,  $\mathcal{C} = \mathcal{C}_{\mathcal{T}}$ .

### D. Problem Formulation

Consider a system  $(\mathcal{T}, \bar{\mathcal{T}}, \mathcal{C}, \Xi)$  that consists of a stationary target  $\mathcal{T}$  located at the origin of the world coordinate frame, and a camera  $\mathcal{C}$  at an unknown pose  $\xi \in \Xi$ , producing an image  $I$  that contains the target. Our goal is to design a framework for estimating the pose of the camera relative to the stationary target, given the produced image. To this end, both the target model  $\mathcal{T}$  and the camera model  $\mathcal{C}$  need to be known a priori. In practice, however,  $\mathcal{C}$  is not directly available and, therefore, must be constructed from the camera's intrinsic parameters, which are typically known. Hence, we define the following problem.

**Problem 1.** *Given the intrinsic parameters of a camera  $\mathcal{C}$  and a target model  $\mathcal{T}$ , design a target-specific camera model  $\mathcal{C}_{\mathcal{T}}$  such that:*

$$\mathcal{C}_{\mathcal{T}}: \Xi \rightarrow \mathbb{B}^{h \times w} \text{ s.t. } \forall \xi \in \Xi : \mathcal{C}(\xi) = I_{\mathcal{T}\xi},$$

where

- $\Xi$  is the pose space of the camera,
- $I_{\mathcal{T}\xi}$  is the ideal image of the target  $\mathcal{T}$  at pose  $\xi$ , and
- $h \times w$  is the size of the image produced by the camera.

In other words, Problem 1 seeks to design a target-specific camera model that reproduces the ideal image of the target at any given pose. With  $\mathcal{C}_{\mathcal{T}}$  in place, we can now define the problem of pose estimation.

**Problem 2.** *Given a system model  $(\mathcal{T}, \bar{\mathcal{T}}, \mathcal{C}_{\mathcal{T}}, \Xi)$  and an image  $I_{\xi} = I(\xi)$ ,  $I_{\xi} \in \mathcal{I}$ , produced by the camera at an unknown pose  $\xi \in \Xi$ , design a pose estimator  $\mathcal{NN}: \mathcal{I}_{\mathcal{T}} \rightarrow \Xi$  such that:*

$$\forall \xi \in \Xi : \hat{\xi} = \mathcal{NN}(I_{\xi}) \text{ and } \|\xi - \hat{\xi}\| \leq \epsilon_{\text{bound}},$$

where

- $I_{\xi}$  is the image produced by the camera at pose  $\xi$ ,
- $\hat{\xi}$  is the estimated pose of the camera, and
- $\epsilon_{\text{bound}} \in \mathbb{R}$  is a small constant.

Note that the error bound  $\epsilon_{\text{bound}}$  quantifies the accuracy of the estimated pose  $\hat{\xi}$ , and is typically given as a specification. Thus, examining the factors that affect the error bound  $\epsilon_{\text{bound}}$  is crucial for designing a robust pose estimator  $\mathcal{NN}$ . Also, since the pose  $\xi$  includes both translational and rotational components, the norm  $\|\cdot\|$  used to quantify the error denotes an appropriate norm on  $\mathbb{R}^6$ , e.g., a weighted  $p$ -norm that accounts for the different units of translation and rotation.

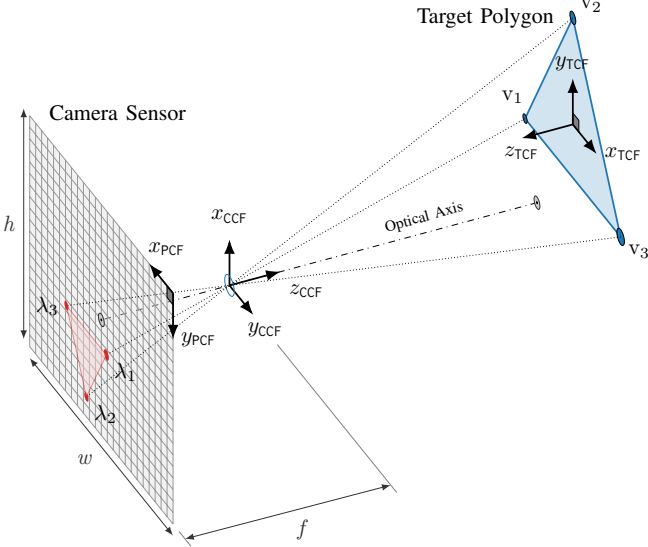


Fig. 4. Ideal pinhole camera illustration, showing the target (TCF), camera (CCF), and pixel (PCF) coordinate frames.  $\lambda_i$  denotes the projection of point  $v_i$  onto the camera sensor.

### III. NN-BASED GENERATIVE GEOMETRIC MODEL

To address Problem 1, we generalize the classical pinhole camera model, originally developed for single points, into a neural network-based camera model with free parameters that capture both intrinsic and extrinsic properties. Because target objects consist of infinitely many points, applying the pinhole model to each point individually is infeasible. Instead, we develop the *generative geometric model* (GGM): a neural-network-like, target-specific model capable of generating images of a target at any given pose. The GGM for a camera and an  $N$ -polygon target object consists of three computational stages: (i) the camera’s *analog behavior* for polygons, which projects the polygon vertices onto the camera sensor; (ii) the camera’s *digital behavior* for polygons, which maps the projected vertices to discrete pixel values in the image; and (iii) the *image composition function*, which combines the pixel values from all polygons to form the final image. In the remainder of this section, we derive the details of these three stages in turn.

#### A. Pinhole Camera Model for Single Point

We begin by revisiting the ideal pinhole camera model for a single point [29]. As shown in Fig. 4, we first introduce the three frames of reference required to describe the image formation process:

- 1) The Target Coordinate Frame (TCF): is attached to the target object, serves as the frame of reference for points in the target.
- 2) The Camera Coordinate Frame (CCF): is attached to the camera, provides the frame of reference for defining the camera’s position and orientation relative to the target.
- 3) The Pixel Coordinate Frame (PCF): is defined over the image plane, serves as the frame of reference for the image produced by the camera.

Using these frames, the mapping of a point on the target to a pixel in the image produced by the camera can be divided into two stages as mentioned earlier. In the first stage, the analog behavior maps the coordinates of a point on the target (expressed relative to the camera) to the coordinates of its projection on the camera sensor (relative to a local frame of reference). Consider a camera pose  $\xi = (x, y, z, \phi, \theta, \psi)$  with respect to the TCF of a target  $\mathcal{T}$ . We then formally define the analog behavior of the camera over a point  $v$  of the target’s 2D plane as follows.

**Definition 5** (Analog Behavior). *The analog behavior of the camera for point  $v$  is a function:*

$$f_{\text{analog}}^v : \Xi \rightarrow \mathbb{R}^3, \quad \xi \mapsto \lambda^{\text{CCF}},$$

where  $\lambda$  is the projection of point  $v$  by the camera lens onto the camera sensor, and  $\lambda^{\text{CCF}} \in \mathbb{R}^3$  is the coordinates of  $\lambda$  in the CCF given the camera pose  $\xi$ .

Note that an analog function  $f_{\text{analog}}^v$  is defined for a specific point  $v$ , and its exact form is determined by the camera’s intrinsic parameters. To this end, we examine two operations that  $v$  undergoes: the transformation of its coordinates from the TCF to the CCF, and the projection of that point by the camera lens onto the camera sensor. The transformation of the coordinates of point  $v$  in the TCF, denoted by  $v^{\text{TCF}}$ , to its coordinates in the CCF, denoted by  $v^{\text{CCF}}$ , is obtained by applying both the rotation and translation matrices [29], denoted  $\mathbf{R}(\xi)$  and  $\mathbf{T}(\xi)$ , respectively, to  $p^{\text{TCF}}$ , where:

$$\mathbf{T}(\xi) = [x \ y \ z]^\top,$$

$$\begin{aligned} \mathbf{R}(\xi) &= \mathbf{R}_z(\psi) \cdot \mathbf{R}_y(\theta) \cdot \mathbf{R}_x(\phi) \\ &= \begin{bmatrix} c_\psi \ c_\theta & c_\psi \ s_\theta \ s_\phi - s_\psi \ c_\phi & c_\psi \ s_\theta \ c_\phi + s_\psi \ s_\phi \\ s_\psi \ c_\theta & s_\psi \ s_\theta \ s_\phi + c_\psi \ c_\phi & s_\psi \ s_\theta \ c_\phi - c_\psi \ s_\phi \\ -s_\theta & c_\theta \ s_\phi & c_\theta \ c_\phi \end{bmatrix}, \end{aligned}$$

and  $\xi = (x, y, z, \phi, \theta, \psi)$ . The transformed point coordinates can then be written as:

$$v^{\text{CCF}} = \mathbf{R}(\xi) \cdot v^{\text{TCF}} + \mathbf{T}(\xi). \quad (1)$$

Next, let  $\lambda$  be the projection of point  $v$  by the camera lens onto the camera sensor. Using the camera intrinsic matrix  $\mathbf{K}$ , the homogeneous pixel coordinates of  $\lambda$  can be obtained as follows:

$$\lambda^{\text{CCF}} = \mathbf{K} \cdot v^{\text{CCF}} = \begin{bmatrix} f & 0 & w/2 \\ 0 & f & h/2 \\ 0 & 0 & 1 \end{bmatrix} \begin{bmatrix} v_x^{\text{CCF}} \\ v_y^{\text{CCF}} \\ v_z^{\text{CCF}} \end{bmatrix}. \quad (2)$$

By substituting (1) into (2), we can define the exact form of the analog function  $f_{\text{analog}}^v$  as follows:

$$f_{\text{analog}}^v(\xi) = \lambda^{\text{CCF}} = \mathbf{K} \cdot (\mathbf{R}(\xi) \cdot v^{\text{TCF}} + \mathbf{T}(\xi)). \quad (3)$$

In the second stage, the digital behavior maps these homogeneous coordinates to discrete pixel values in the image. We formally define the digital behavior as follows.

**Definition 6** (Digital Behavior). *The digital behavior of the camera for a point  $v$  at pixel  $q \in \mathbb{Z}^2$  in the image is a function:*

$$f_{\text{digital}}^{v,q} : \lambda^{\text{CCF}} \mapsto I(q),$$

where  $\lambda^{\text{CCF}}$  is the homogeneous coordinates of  $v$  in the CCF, obtained from the analog stage; and  $I(q) \in \mathbb{B}$  is the value at pixel  $q$  in the image.

Note that the digital function  $f_{\text{digital}}^{\text{V},q}$  is defined for a specific point  $v$  and pixel  $q$ . To realize this function, we compute the corresponding pixel coordinates in the PCF that correspond to  $\lambda^{\text{CCF}}$ , denoted by  $\lambda^{\text{PCF}}$ , by rounding the normalized coordinates of  $\lambda^{\text{CCF}}$  to the nearest integer:

$$\lambda^{\text{PCF}} = \left( \lfloor \lambda_x^{\text{CCF}} / \lambda_z^{\text{CCF}} \rfloor, \lfloor \lambda_y^{\text{CCF}} / \lambda_z^{\text{CCF}} \rfloor \right).$$

Therefore, the projection of a single point  $v$  results in setting the pixel value at  $\lambda^{\text{PCF}}$  to 1 in the image produced by the camera provided that  $\lambda^{\text{PCF}}$  lies within the image boundaries. Consequently, we can define the exact form of the digital function for any pixel  $q = (q_x, q_y)$  as follows:

$$f_{\text{digital}}^{\text{V},q}(\lambda^{\text{CCF}}) = \begin{cases} 1 & \text{if } \lambda^{\text{PCF}} = q, 1 \leq q_x \leq w, 1 \leq q_y \leq h, \\ 0 & \text{otherwise.} \end{cases} \quad (4)$$

### B. Generalized Camera Model for Convex Polygons

So far we have derived the exact form of the analog and digital functions (3) and (4) for mapping a single point  $v$  to the image produced by the camera. However, a target object has virtually an infinite number of points, making it infeasible to apply the analog and digital functions to each point individually. To address this issue, we derive a procedure that efficiently maps a target object to the image produced by the camera by leveraging the convex polygon-based representation of target objects that we introduced earlier in Definition 1.

We start by defining the analog behavior for a convex polygon  $V$  as the collection of analog functions applied to each vertex  $v \in V$ , that is:

$$f_{\text{analog}}^V : \Xi \rightarrow (\mathbb{R}^3)^n, \quad \xi \mapsto (\lambda_1^{\text{CCF}}(\xi), \dots, \lambda_n^{\text{CCF}}(\xi)),$$

where  $\lambda_j^{\text{CCF}}(\xi) := f_{\text{analog}}^{\text{V},j}(\xi) \in \mathbb{R}^3$  denotes the (homogeneous) image-plane coordinates of the projection of  $v_j$  at pose  $\xi$ . We denote the pose-dependent collection of projected vertices by

$$\Lambda^{\text{CCF}}(\xi) := \{\lambda_1^{\text{CCF}}(\xi), \dots, \lambda_n^{\text{CCF}}(\xi)\}.$$

The digital behavior for a convex polygon, however, must consider all the points within the polygon's convex hull rather than just its vertices. Hence, we extend the definition of the digital behavior to convex polygons as follows.

**Definition 7** (Digital Behavior for Convex Polygons). *The digital behavior of the camera for a convex polygon  $V$  at pixel  $q \in \{1, \dots, h\} \times \{1, \dots, w\}$  in the image produced by the camera is a function:*

$$f_{\text{digital}}^{\text{V},q} : \Lambda^{\text{CCF}} \mapsto I(q) \text{ s.t. } I(q) = \begin{cases} 1 & \text{if } q \in \text{Conv}(\Lambda^{\text{CCF}}), \\ 0 & \text{otherwise,} \end{cases}$$

where  $\Lambda^{\text{CCF}} = \{\lambda_1^{\text{CCF}}, \dots, \lambda_n^{\text{CCF}}\}$  is the set of homogeneous image coordinates of the projections of the vertices of  $V$ , and  $\text{Conv}(\Lambda^{\text{CCF}})$  is the convex hull of  $\Lambda^{\text{CCF}}$ .

Unlike the single-point case, where only one pixel is activated, the polygon digital behavior activates all pixels inside

the convex hull of the projected vertices, subject to the field-of-view constraints of the image. Consequently, instead of applying the digital function to each point in the polygon individually, we can now obtain the image of the polygon by only applying the polygon digital function at each pixel in the image. To realize  $f_{\text{digital}}^{\text{V},q}$ , we implement the condition  $q \in \text{Conv}(\Lambda^{\text{CCF}})$  by applying an orientation test based on the cross product of the pixel coordinates with each edge of the projected polygon  $\Lambda^{\text{CCF}}$ . For a pixel  $q = (q_x, q_y)$ , we start by picking the first two projected vertices  $\lambda_1, \lambda_2 \in \Lambda^{\text{CCF}}$ , and compute the cross product of the vectors  $\lambda_1 \lambda_2$  and  $\lambda_1 q$  as follows:

$$\begin{aligned} C_q(1, 2) &\triangleq \overrightarrow{\lambda_1 \lambda_2} \times \overrightarrow{\lambda_1 q} \\ &= q_y (\lambda_{2x} - \lambda_{1x}) - q_x (\lambda_{2y} - \lambda_{1y}) \\ &\quad + (\lambda_{2x} \lambda_{1y} - \lambda_{2y} \lambda_{1x}). \end{aligned} \quad (5)$$

We repeat this computation for each consecutive pair of vertices  $C_q(i, n-1)$ ,  $i = 1 \dots n$ , and for the closing edge  $C_q(n, 1)$ . If all cross products share the same sign, then the condition  $q \in \text{Conv}(\Lambda^{\text{CCF}})$  holds, and the pixel is activated. That is:

$$f_{\text{digital}}^{\text{V},q}(\Lambda^{\text{CCF}}) = \begin{cases} 1 & \text{if } \forall i \in \{1, \dots, n-1\} : \\ & \text{sgn}(C_q(i, i+1)) = \text{sgn}(C_q(n, 1)) \\ 0 & \text{otherwise.} \end{cases} \quad (6)$$

Finally, by applying (5) and (6) at every pixel location, we can construct the image of the polygon as follows:

$$I_V(\xi) = \left[ f_{\text{digital}}^{\text{V},(q_x, q_y)}(\Lambda^{\text{CCF}}) \right]_{q_x=1, q_y=1}^{h, w}. \quad (7)$$

This procedure allows for efficient generation of the polygon image without evaluating the analog and digital behaviors for infinitely many interior points.

**Example 2.** Fig. 5 illustrates the orientation test for determining whether a pixel  $q$  lies within the convex hull of the projected vertices  $\lambda_1, \lambda_2, \lambda_3$  of the convex polygon from Fig. 4. In this example, the signs of the cross products  $C_q(1, 2)$ ,  $C_q(2, 3)$ , and  $C_q(3, 1)$  is depicted for each pixel, where the color of each pixel indicates the sign of the corresponding cross product at that pixel. For example, for  $q = (12, 10)$ :

$C_{(12,10)}(1, 2) < 0$ ,  $C_{(12,10)}(2, 3) < 0$ ,  $C_{(12,10)}(3, 1) > 0$ , so  $f_{\text{digital}}^{\text{V},(12,10)}(\Lambda^{\text{CCF}}) = 0$ . However, for  $q = (15, 14)$ , we have:

$$C_{(15,14)}(1, 2), C_{(15,14)}(2, 3), C_{(15,14)}(3, 1) < 0,$$

so  $f_{\text{digital}}^{\text{V},(15,14)}(\Lambda^{\text{CCF}}) = 1$  since all cross products share the same sign.

### C. Compositional Model for $N$ -Polygon Targets

The analog and digital behaviors defined so far describe how to generate the image of a single convex polygon  $V_i$  at a given camera pose  $\xi$ . We now extend this formulation to entire target objects, which are represented as collections of polygons  $\mathcal{T} = \{V_1, \dots, V_N\}$ . For each polygon  $V_i \in \mathcal{T}$ , the analog and digital behaviors yield a binary image  $I_{V_i}(\xi)$ .

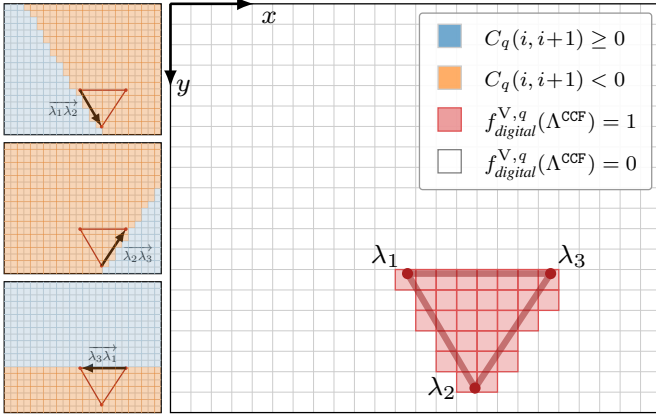


Fig. 5. Orientation test for determining whether each pixel  $q$  lies within the convex hull of the projected vertices  $\lambda_1, \lambda_2, \lambda_3$  of the convex polygon from Fig. 4. The sign of the cross products are shown for  $C_q(1, 2), C_q(2, 3)$ , and  $C_q(3, 1)$ .

TABLE I. Image Composition Operator Semantics

$I_{\mathcal{T}}(\xi) := \mathcal{E}_{\mathcal{T}}(I_{V_1}(\xi), \dots, I_{V_N}(\xi))$	
$\neg I := \mathbf{1} - I$	(Negation)
$(I_1 \vee I_2) := \max\{I_1, I_2\} = \min\{1, I_1 + I_2\}$	(Union)
$(I_1 \wedge I_2) := \min\{I_1, I_2\} = \max\{0, I_1 + I_2 - 1\}$	(Intersection)
$(I_1 \oplus I_2) := (I_1 \vee I_2) \wedge \neg(I_1 \wedge I_2)$	(Difference)

The image of the target  $\mathcal{T}$  is then obtained by applying a composition expression  $\mathcal{E}$  over the polygon images, generated by the grammar

$$\mathcal{E} ::= I_{V_i}(\xi) \mid \neg \mathcal{E} \mid \mathcal{E}_1 \vee \mathcal{E}_2 \mid \mathcal{E}_1 \wedge \mathcal{E}_2 \mid \mathcal{E}_1 \oplus \mathcal{E}_2,$$

where  $\vee$ ,  $\wedge$ , and  $\oplus$  denote element-wise Boolean operations OR, AND, and XOR, respectively. The semantics of these operators are defined in Table I. Here, all operations are applied pixelwise on the binary images produced by the analog and digital behaviors. At the geometric level, these correspond respectively to the union, intersection, and symmetric difference of the polygons' projections. Thus, the compositional model provides a general mechanism to assemble the target image from its constituent polygons.

#### D. Geometric Generative Model (GGM) for N-Polygon Target

As shown in Fig. 6(a), the (GGM) for a target object  $\mathcal{T}$  involves three stages: the analog behavior, the digital behavior, and the image composition function. We now discuss the implementation of each stage as a NN-based computational graph (CG). Fig. 6(b) illustrates the CG for the analog behavior of a single vertex  $v$ , which directly implements the analog function in (3). The CG takes as input the camera pose  $\xi$  and returns the homogeneous image coordinates  $\lambda^{CCF}$  of the projection of  $v$  in the CCF. The hidden layers of the CG implements the non-linear sinusoidal and multiplicative operations in (1), followed by the normalization and linear operations in (2). Those computations are characterized by two sets of fixed parameters: the intrinsic parameters of the camera, including  $f$ ,  $w$ ,  $h$ ; and the 3D coordinates of the vertex  $v^{TCF} = (v_x, v_y, 0)$  in the TCF. Subsequently, each

TABLE II. GGM layers for an  $n$ -polygon.

Layer	Description	Activation	Size
L0	Input	None	$2n$ (shared)
L1	Cross product	Linear	$h \times w \times n$
L2	Absolute value	ReLU (Paired)	$h \times w \times (2n + 2)$
L3	Summation	Linear	$h \times w \times 2$
L4	Output (Binary)	ReLU (Threshold)	$h \times w$

vertex requires a separate CG with identical structure but different parameters. Fig. 6(c) illustrates the CG for the digital behavior of a single polygon  $V_i$  (of size  $n_i = 4$ ) at a single pixel  $q = (q_x, q_y)$ , implementing the sign test in (6). The input layer consists of the projected 2D coordinates of the polygon vertices in the CCF, i.e.,  $\lambda_1^{CCF}, \dots, \lambda_{n_i}^{CCF}$ , where  $\lambda_j^{CCF} = (\lambda_{x_j}^{CCF}, \lambda_{y_j}^{CCF})$ , resulting in an input size of  $2n_i$ . The output of the NN is a binary value indicating whether the pixel  $q$  lies inside the projection of the polygon in the image plane. As shown in Table II, the GGM subnetwork  $\mathcal{NN}^{V_i, q}$  includes three hidden layers, namely L1, L2, and L3, that model the geometric relations between the polygon vertices and the image pixels. The layer L1 computes the cross product in (5) for each pair of consecutive input projections:

$$a_1^{(1)} = q_y (\lambda_{2x} - \lambda_{1x}) - q_x (\lambda_{2y} - \lambda_{1y}) + (\lambda_{2x} \lambda_{1y} - \lambda_{2y} \lambda_{1x}),$$

where  $a_1^{(1)}$  is the output of the first node in L1. To determine whether the pixel  $q$  lies within the polygon, and hence its value, we implement the orientation test in (6):

$$\text{sgn}(a_i^{(1)}) = \text{sgn}(a_{i+1}^{(1)}) \iff \sum_{i=1}^n |a_i^{(1)}| - \left| \sum_{i=1}^n a_i^{(1)} \right| = 0.$$

That is, if the sum of the absolute values of the cross products equals the absolute value of their sum, then all cross products share the same sign and, consequently, the pixel  $q$  lies within the polygon. This test is implemented in the subsequent layers, L2, L3, and L4.

For each output of L1,  $a_i^{(1)}$ , both the value and its negation are fed into two separate ReLU nodes in L2:

$$a_{ia}^{(2)} = \max\{a_i^{(1)}, 0\}, \quad a_{ib}^{(2)} = \max\{-a_i^{(1)}, 0\}.$$

Either  $a_{ia}^{(2)}$  or  $a_{ib}^{(2)}$  yields the absolute value of  $a_i^{(1)}$ , while the other yields zero. Effectively, their sum equals the absolute value of  $a_i^{(1)}$ :

$$a_{ia}^{(2)} + a_{ib}^{(2)} = \max\{a_i^{(1)}, 0\} + \max\{-a_i^{(1)}, 0\} = |a_i^{(1)}|.$$

This summation is performed for all outputs of L2 using the first neuron of L3 to compute the sum of the absolute values of the cross products:

$$a_1^{(3)} = \sum_{i=1}^n (a_{ia}^{(2)} + a_{ib}^{(2)}) = \sum_{i=1}^n |a_i^{(1)}|.$$

Similarly, the last two ReLU nodes in L2 compute the positive and negative values of the sum of the cross products:

$$a_{(n+1)a}^{(2)} = \sum_{i=1}^n a_i^{(1)}, \quad a_{(n+1)b}^{(2)} = - \sum_{i=1}^n a_i^{(1)}.$$

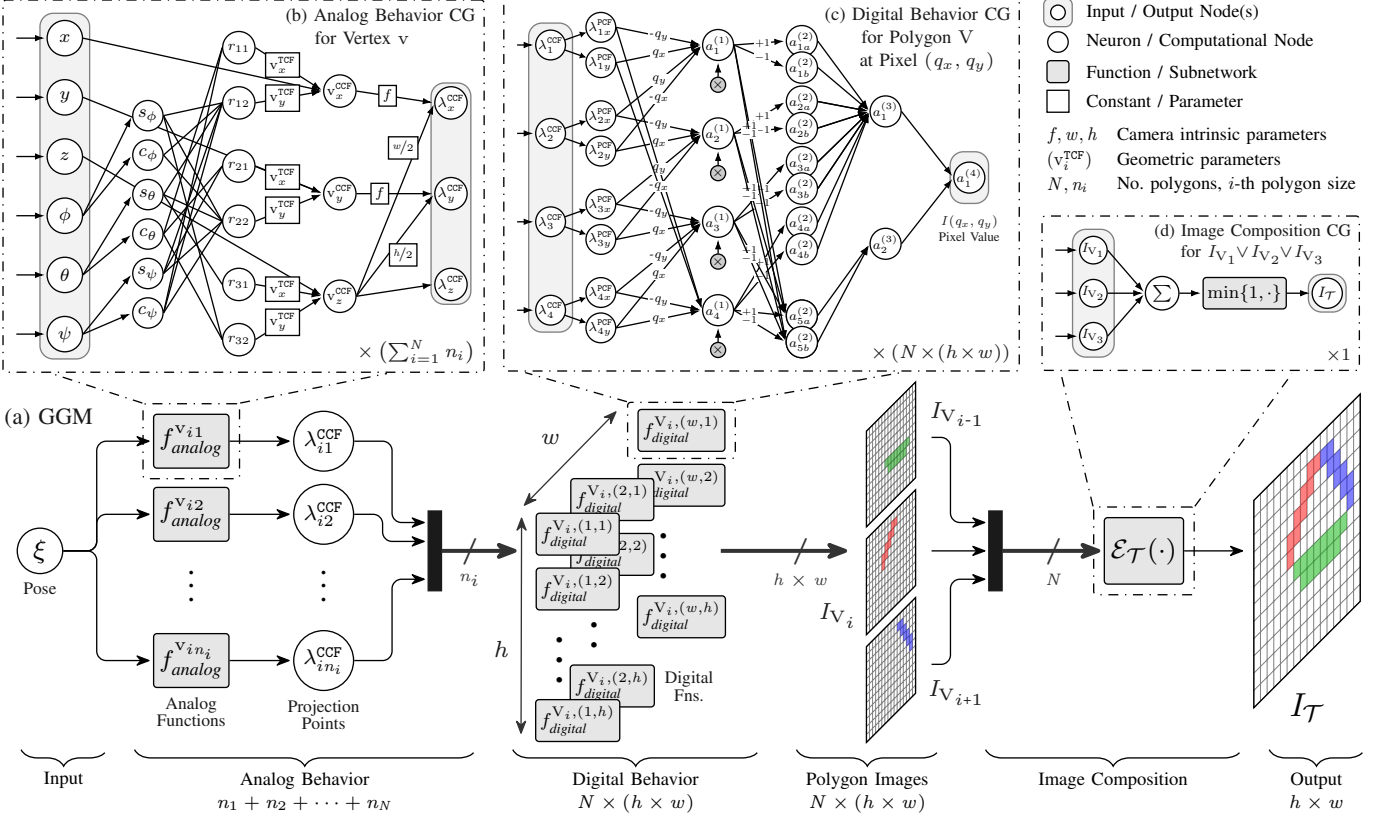


Fig. 6. Computational graph (CG) of (a) the GGM for generating the image  $I_{\mathcal{T}}$  of a target object  $\mathcal{T}$  at camera pose  $\xi = (x, y, z, \phi, \theta, \psi)$ ; (b) the analog behavior CG for vertex  $v$ ; (c) the digital behavior CG for polygon  $V_i$  (of size  $n_i = 4$ ) at pixel  $q = (q_x, q_y)$ ; and (d) the composition function CG for combining the images of  $N$  polygons, where  $I_{\mathcal{T}}(\xi) = I_{V_1}(\xi) \vee I_{V_2}(\xi) \vee I_{V_3}(\xi)$ . Some nodes and edges are consolidated, simplified or omitted for clarity.

The second neuron in L3 is then used to compute the absolute value of this sum:

$$a_2^{(3)} = a_{(n+1)a}^{(2)} + a_{(n+1)b}^{(2)} = \left| \sum_{i=1}^n a_i^{(1)} \right|.$$

Finally, the output layer L4 comprises a single neuron that outputs:

$$a^{(4)} = \begin{cases} 1 & \text{if } a_1^{(3)} = a_2^{(3)}, \\ 0 & \text{otherwise,} \end{cases}$$

that is, the output of L4 is used to set the pixel value  $I(q)$  to 1 if the pixel  $q$  is inside the polygon, and 0 otherwise. Each pair of a polygon  $V_i$  and a pixel  $q$  requires a separate CG with identical structure but different parameters; thus, a total of  $N \times h \times w$  digital behavior CGs are needed to generate the image of  $\mathcal{T}$ , where each group of  $h \times w$  CGs generates the image of the corresponding polygon  $V_i$ . Fig. 6(d) illustrates the CG for the composition function that combines the images of  $N$  polygons. In this example, the target  $\mathcal{T}$  consists of three polygons, where its geometry is defined by the union of the images of the constituent polygons. Thus, the CG implements the expression  $I_{\mathcal{T}}(\xi) = I_{V_1}(\xi) \vee I_{V_2}(\xi) \vee I_{V_3}(\xi)$  using the  $\min\{1, \cdot\}$  semantics listed in Table I by summing the outputs of the three polygon subnetworks and capping the pixel values

using  $\min\{1, \cdot\}$ :

$$\begin{aligned} I_{\mathcal{T}}(\xi) &= I_{V_1}(\xi) \vee I_{V_2}(\xi) \vee I_{V_3}(\xi) \\ &= \min\{1, I_{V_1}(\xi) + \min\{1, I_{V_2}(\xi) + I_{V_3}(\xi)\}\} \\ &= \min\{1, I_{V_1}(\xi) + I_{V_2}(\xi) + I_{V_3}(\xi)\}. \end{aligned}$$

Note that the architecture of the image composition CG depends on the exact expression  $\mathcal{E}$  used to combine the polygon images.

#### IV. CERTIFIED VISION-BASED POSE ESTIMATION FOR UNCLUTTERED ENVIRONMENTS

We now take the first step towards addressing the general problem of vision-based pose estimation described in Problem 2. Specifically, we consider the case where the camera is capturing images of a target object in an uncluttered environment (see Definition 3).

##### A. Problem Overview

Consider a system  $(\mathcal{T}, \bar{\mathcal{T}}, \mathcal{C}_{\mathcal{T}}, \Xi)$  in an uncluttered environment where the target object  $\mathcal{T}$  is the only one present in the scene captured by the camera, i.e.,  $\bar{\mathcal{T}} = \emptyset$  and  $I(\xi) = I_{\mathcal{T}}(\xi)$  by definition. This assumption relaxes the problem of pose estimation by eliminating the need to detect and identify multiple objects within the image. We can now formalize the relaxed version of Problem 2 as follows.

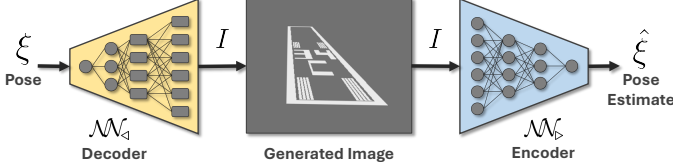


Fig. 7. Decoder-encoder framework for designing a certifiable image-to-pose estimator.

**Problem 3.** Given a system  $(\mathcal{T}, \overline{\mathcal{T}}, \mathcal{C}_{\mathcal{T}}, \Xi_{\mathcal{T}})$ , where  $\overline{\mathcal{T}} = \emptyset$ , and  $\Xi_{\mathcal{T}} \subseteq \Xi$  is the pose space region where  $\mathcal{T}$  is fully visible, design a pose estimator  $\mathcal{NN}: \mathcal{I}_{\mathcal{T}} \rightarrow \Xi$  such that:

$$\max_{\xi \in \Xi_{\mathcal{T}}} \|\xi - \mathcal{NN}(I_{\xi})\| \leq \epsilon_{\text{bound}},$$

where  $I_{\xi} = I(\xi)$  is the image produced by the camera at pose  $\xi$ , and  $\epsilon_{\text{bound}} \in \mathbb{R}_{\geq 0}$  is a user-defined error bound.

In other words, the goal is to design a pose estimator that, given an image where the target object is fully visible, can estimate the camera's pose with a certified bound on the estimation error.

### B. GGM-based Decoder-Encoder Framework

We address Problem 3 by proposing a two-stage framework for designing a certifiable image-to-pose estimator. As shown in Fig. 7, the proposed framework for designing a certifiable image-to-pose estimator consists of two main components. The first component, the *decoder*, is a GGM  $\mathcal{NN}_{\triangleleft}: \Xi_{\mathcal{T}} \rightarrow \mathcal{I}$  for generating synthetic images of the target object for any given pose  $\xi \in \Xi_{\mathcal{T}}$ , where  $\Xi_{\mathcal{T}}$  is the bounded pose space of the camera. The second component, the *encoder*  $\mathcal{NN}_{\triangleright}: \mathcal{I} \rightarrow \Xi_{\mathcal{T}}$ , is a neural network that takes an ideal image of the target object as input and outputs the estimated pose of the camera.

The process of designing the encoder is outlined in Algorithm 1. First, a GGM-based decoder  $\mathcal{NN}_{\triangleleft}$  is designed for the geometric properties of the target object and the intrinsic parameters of the camera. Next, the GGM-based decoder is utilized to train an encoder  $\mathcal{NN}_{\triangleright}$  to learn the mapping between the ideal image of the target object and the pose of the camera at which the image was captured. Akin to autoencoders—albeit the order of the encoder and decoder is flipped as shown in Fig. 7—we use reconstruction loss between the input to the decoder and the output of the encoder:

$$\mathcal{L}_{\text{Encoder}} = \|\xi - \hat{\xi}\| = \|\xi - \mathcal{NN}_{\triangleright}(\mathcal{NN}_{\triangleleft}(\xi))\|$$

Next, the GGM-based decoder is utilized to generate a dataset of pose-image pairs  $\mathcal{D}_{\text{test}} = \{(\xi_i, I_i)\}_{i=1}^N \subset \Xi_{\mathcal{T}} \times \mathcal{I}$ . For our design, it is crucial that the dataset  $\mathcal{D}_{\text{test}}$  is constructed by sampling poses  $\xi$  over a grid of size  $\eta$ . This dataset is then used to test the encoder  $\mathcal{NN}_{\triangleright}$  and evaluate the empirical error  $\epsilon$  which will then be used to establish the worst case upper bound  $\epsilon_{\text{bound}}$  on the trained encoder.

### C. Formal Guarantees on Encoder Performance

Before we discuss the formal guarantees of the proposed decoder-encoder, we present a necessary condition for the well-posedness of Problem 3. In particular, for the existence of

**Algorithm 1:** Decoder-Encoder Framework for Certifiable Pose Estimation

**Input:**  $\mathcal{T}$ , target geometry;  $\Xi_{\mathcal{T}}$ , bounded pose space;  
**Output:**  $\mathcal{NN}_{\triangleright}$ , certified image-to-pose estimator

**1 Stage 1: Decoder**

- 2 Construct GGM  $\mathcal{NN}_{\triangleleft}: \Xi_{\mathcal{T}} \rightarrow \mathcal{I}_{\mathcal{T}}$  for  $\mathcal{T}$  and  $\mathcal{C}$
- 3 Compute Lipschitz constant  $L_{\mathcal{NN}_{\triangleleft}}$  of  $\mathcal{NN}_{\triangleleft}$
- 4 Generate testing dataset  $\mathcal{D}_{\text{test}} \leftarrow \emptyset$
- 5 Select grid size  $\eta$
- 6 **for**  $i = 1, \dots, \eta^6$  **do**
- 7     Sample  $\xi_i$  from a grid over  $\Xi_{\mathcal{T}}$  with resolution  $\eta$
- 8     Obtain image from GGM  $I_i \leftarrow \mathcal{NN}_{\triangleleft}(\xi_i)$
- 9      $\mathcal{D}_{\text{test}} \leftarrow \mathcal{D}_{\text{test}} \cup \{(\xi_i, I_i)\}$

**10 Stage 2: Encoder**

- 11 Compute Lipschitz constant  $L_{\mathcal{NN}_{\triangleright}}$  of  $\mathcal{NN}_{\triangleright}$
- 12 Sample randomly from  $\Xi_{\mathcal{T}}$  and train the encoder  $\mathcal{NN}_{\triangleright}: \mathcal{I}_{\mathcal{T}} \rightarrow \Xi_{\mathcal{T}}$  using the reconstruction loss:
- 13  $\mathcal{L}_{\text{Encoder}} = \|\xi - \hat{\xi}\| = \|\xi - \mathcal{NN}_{\triangleright}(\mathcal{NN}_{\triangleleft}(\xi))\|$
- 14 Evaluate  $\mathcal{NN}_{\triangleright}$  on test dataset  $\mathcal{D}_{\text{test}}$
- 15 Compute empirical error  $\epsilon \leftarrow \max_{(\xi_i, I_i) \in \mathcal{D}_{\text{test}}} \|\xi_i - \mathcal{NN}_{\triangleright}(I_i)\|$
- 16 Compute certified bound  $\epsilon_{\text{bound}} \leftarrow (\eta + \delta)(L_{\mathcal{NN}_{\triangleleft}} L_{\mathcal{NN}_{\triangleright}} + 1) + \epsilon$
- 17 **return**  $\mathcal{NN}_{\triangleright}$ ,  $\epsilon_{\text{bound}}$

an encoder that provides unique pose estimates from images, the mapping between the image space and the pose space must be injective. This means that for each image generated by the decoder, there should be a unique corresponding pose in the pose space. Conversely, if two different poses produce the same image, the encoder cannot distinguish between them, leading to ambiguity in the pose estimation.

**Definition 8** (Injectivity Condition). *The decoder  $\mathcal{NN}_{\triangleleft}: \Xi_{\mathcal{T}} \rightarrow \mathcal{I}$  is said to be injective if:*

$$\forall \xi_1, \xi_2 \in \Xi_{\mathcal{T}}, \xi_1 \neq \xi_2 \implies \mathcal{NN}_{\triangleleft}(\xi_1) \neq \mathcal{NN}_{\triangleleft}(\xi_2). \quad (8)$$

Unfortunately, Definition 8 is very restrictive and can not be applied to this problem due to the topological mismatch between the domain and codomain of  $\mathcal{NN}_{\triangleleft}$ . While the pose space  $\Xi_{\mathcal{T}}$  is a continuous space, the image space  $\mathcal{I}$  is intrinsically discrete, constrained by finite pixel quantization. Consequently, the GGM-based decoder  $\mathcal{NN}_{\triangleleft}: \Xi_{\mathcal{T}} \rightarrow \mathcal{I}$  functions as a quantization operator, rendering strict injectivity mathematically impossible; distinct poses that differ by sub-pixel perturbations will inevitably map to the identical images. As a result, the pre-image  $\mathcal{NN}_{\triangleleft}^{-1}(I)$  of an image  $I$  is never a singleton, but rather a “set” of indistinguishable poses. Therefore, the traditional condition of injectivity in Definition 8 is ill-posed for this setting. To establish rigorous guarantees for the inverse map  $\mathcal{NN}_{\triangleright}$ , we must relax this requirement to  $\delta$ -identifiability, replacing the notion of unique recovery with that of recovery within a strictly bounded diameter of uncertainty.

**Definition 9** ( $\delta$ -Identifiability). *The decoder  $\mathcal{NN}_{\triangleleft}: \Xi_{\mathcal{T}} \rightarrow \mathcal{I}$  is said to be  $\delta$ -identifiable if, for any pair of poses  $\xi_1, \xi_2 \in \Xi_{\mathcal{T}}$ , the following implication holds:*

$$\mathcal{NN}_{\triangleleft}(\xi_1) = \mathcal{NN}_{\triangleleft}(\xi_2) \implies \|\xi_1 - \xi_2\| \leq \delta. \quad (9)$$

**Assumption 1** ( $\delta$ -Identifiable GGM Decoder). *We assume that the GGM-based decoder  $\mathcal{NN}_{\triangleleft}$  is  $\delta$ -Identifiable (i.e., according to Definition 9) over  $\Xi_{\mathcal{T}}$ .*

A violation of Assumption 1 occurs when distinct camera poses produce identical or indistinguishable images. Examples include symmetric target objects viewed from different angles, or poses outside the camera's field of view where the target object is not visible.

We now establish formal guarantees on the accuracy of the NN-based encoder  $\mathcal{NN}_{\triangleright}$  as follows.

**Theorem 1** (Estimation Error Bounds). *Consider a system  $(\mathcal{T}, \bar{\mathcal{T}}, \mathcal{C}_{\mathcal{T}}, \Xi)$  where  $\bar{\mathcal{T}} = \emptyset$ , i.e., an uncluttered environment. Given a neural network encoder  $\mathcal{NN}_{\triangleright}$  trained using Algorithm 1. Let Assumption 1 holds over  $\Xi_{\mathcal{T}}$ , then the following bound on the pose estimation error holds:*

$$\max_{\xi \in \Xi_{\mathcal{T}}} \|\xi - \mathcal{NN}_{\triangleright}(I_{\xi})\| \leq (\delta + \eta)(L_{\triangleleft}L_{\triangleright} + 1) + \epsilon,$$

where  $L_{\triangleleft}$  and  $L_{\triangleright}$  are the Lipschitz constants of the decoder and encoder networks, respectively, and  $\eta$  is the grid size used to generate the test dataset  $\mathcal{D}_{\text{test}}$  in Algorithm 1. Finally,  $\epsilon$  is the maximum empirical error over the test dataset  $\mathcal{D}_{\text{test}}$ , i.e.,

$$\epsilon = \max_{(\xi_i, I_i) \in \mathcal{D}_{\text{test}}} \|\xi_i - \mathcal{NN}_{\triangleright}(I_i)\|.$$

**Remark 1.** *Theorem 1 provides a worst-case upper bound on the pose estimation error over the entire bounded pose space  $\Xi_{\mathcal{T}}$ . This is in contrast to classical machine learning error bounds, which typically provide probabilistic guarantees over only the poses present in the training dataset. The bound in Theorem 1 is deterministic and holds for all poses within the specified pose space (even for poses that were not present in the training data), offering a stronger assurance of performance for safety-critical applications, compared to probabilistic bounds provided in standard machine learning literature, which is limited to the training samples.*

*Proof.* The proof of Theorem 1 relies on the properties of Lipschitz continuous functions and the composition of such functions. We start by noting that the encoder  $\mathcal{NN}_{\triangleright}$  and decoder  $\mathcal{NN}_{\triangleleft}$  are both Lipschitz continuous, which implies that small changes in the input pose will result in bounded changes in the output pose.

First, let  $\xi, \hat{\xi} \in \Xi_{\mathcal{T}}$  be the true pose and the estimated pose, respectively. Also, let  $I_{\mathcal{T}}(\xi)$  be the ideal image of the target object at pose  $\xi$ , and  $I_{\xi}$  be the image captured by the camera at pose  $\xi$ . Since an uncluttered environment is assumed, from Definition 3, we have:

$$I_{\xi} = I(\xi) = I_{\mathcal{T}}(\xi).$$

That is, the image captured by the camera is equal to the image generated by the decoder at the same pose  $\xi$ . We can then write the encoder's output as:

$$\hat{\xi} = \mathcal{NN}_{\triangleright}(I_{\xi}) = \mathcal{NN}_{\triangleright}(I_{\mathcal{T}}(\xi)).$$

We can then express the estimation error as:

$$\begin{aligned} \|\hat{\xi} - \xi\| &= \|\mathcal{NN}_{\triangleright}(I_{\xi}) - \xi\| \\ &= \|\mathcal{NN}_{\triangleright}(I_{\mathcal{T}}(\xi)) - \xi\|. \end{aligned} \quad (10)$$

By Assumption 1, any pose  $\xi'$  such that  $\|\xi - \xi'\| \leq \delta$  can create the same image, i.e.,  $I_{\mathcal{T}}(\xi) = \mathcal{NN}_{\triangleleft}(\xi) = \mathcal{NN}_{\triangleleft}(\xi')$ . Hence, by into (10), we can rewrite the estimation error as:

$$\|\hat{\xi} - \xi\| \leq \max_{\substack{\xi_{\delta} \in \Xi_{\mathcal{T}} \\ \|\xi - \xi_{\delta}\| \leq \delta}} \|\mathcal{NN}_{\triangleright}(\mathcal{NN}_{\triangleleft}(\xi_{\delta})) - \xi\|. \quad (11)$$

Given a test dataset  $\mathcal{D}_{\text{test}}$  of pose-image pairs with poses sampled over a grid with sample step  $\eta$  and maximum test error  $\epsilon$ , there exists a test sample  $(\xi', I_{\xi'}) \in \mathcal{D}_{\text{test}}$  such that:

$$\|\xi - \xi'\| \leq \eta, \quad \|\mathcal{NN}_{\triangleright}(I_{\xi'}) - \xi'\| \leq \epsilon, \quad (12)$$

where  $I_{\xi'} = \mathcal{NN}_{\triangleleft}(\xi')$ . We can now decompose the estimation error in (11) using the triangle inequality and the constraints in (12):

$$\begin{aligned} \|\hat{\xi} - \xi\| &\leq \max_{\substack{\xi_{\delta} \in \Xi_{\mathcal{T}} \\ \|\xi - \xi_{\delta}\| \leq \delta}} \|\mathcal{NN}_{\triangleright}(\mathcal{NN}_{\triangleleft}(\xi_{\delta})) - \xi\| \\ &\leq \max_{\substack{\xi_{\delta} \in \Xi_{\mathcal{T}} \\ \|\xi - \xi_{\delta}\| \leq \delta}} \|\mathcal{NN}_{\triangleright}(\mathcal{NN}_{\triangleleft}(\xi_{\delta})) - \mathcal{NN}_{\triangleright}(I_{\xi'})\| \\ &\quad + \|\mathcal{NN}_{\triangleright}(I_{\xi'}) - \xi'\| \\ &\leq \max_{\substack{\xi_{\delta} \in \Xi_{\mathcal{T}} \\ \|\xi - \xi_{\delta}\| \leq \delta}} \|\mathcal{NN}_{\triangleright}(\mathcal{NN}_{\triangleleft}(\xi_{\delta})) - \mathcal{NN}_{\triangleright}(I_{\xi'})\| + \epsilon + \eta. \end{aligned} \quad (13)$$

Since  $\mathcal{NN}_{\triangleleft}$  and  $\mathcal{NN}_{\triangleright}$  are Lipschitz continuous, we have:

$$\begin{aligned} \|\mathcal{NN}_{\triangleleft}(\xi_{\delta}) - \mathcal{NN}_{\triangleleft}(\xi')\| &\leq L_{\triangleleft}\|\xi_{\delta} - \xi'\|, \\ \|\mathcal{NN}_{\triangleright}(\mathcal{NN}_{\triangleleft}(\xi_{\delta})) - \mathcal{NN}_{\triangleright}(\mathcal{NN}_{\triangleleft}(\xi'))\| &\leq L_{\triangleright}\|\mathcal{NN}_{\triangleleft}(\xi_{\delta}) - \mathcal{NN}_{\triangleleft}(\xi')\|. \end{aligned}$$

Therefore:

$$\begin{aligned} \max_{\substack{\xi_{\delta} \in \Xi_{\mathcal{T}} \\ \|\xi - \xi_{\delta}\| \leq \delta}} \|\mathcal{NN}_{\triangleright}(\mathcal{NN}_{\triangleleft}(\xi_{\delta})) - \mathcal{NN}_{\triangleright}(\mathcal{NN}_{\triangleleft}(\xi'))\| &\leq L_{\triangleright}L_{\triangleleft}\|\xi_{\delta} - \xi'\| \\ &\leq L_{\triangleright}L_{\triangleleft}(\|\xi_{\delta} - \xi\| + \|\xi - \xi'\|) \\ &\leq L_{\triangleleft}L_{\triangleright}(\delta + \eta). \end{aligned} \quad (14)$$

Substituting (14) into (13), we obtain:

$$\begin{aligned} \|\hat{\xi} - \xi\| &\leq L_{\triangleleft}L_{\triangleright}(\delta + \eta) + \epsilon + \eta \\ &\leq (\delta + \eta)(L_{\triangleleft}L_{\triangleright} + 1) + \epsilon. \end{aligned}$$

Since we considered an arbitrary pose  $\xi \in \Xi_{\mathcal{T}}$ , the bound holds for all poses in the space. This establishes the desired bound on the estimation error, completing the proof for Theorem 1.  $\square$

Since the constants  $\delta$  and  $\eta$  are typically small, the bound established in Theorem 1 indicates that the estimation error is dominated by two factors:

- 1) The Lipschitz constants  $L_{\triangleleft}$  and  $L_{\triangleright}$ , which capture the sensitivity of the mapping to perturbations in the input pose and image, respectively. While the Lipschitz constant  $L_{\triangleleft}$  depends on the GGM and the complexity of



Fig. 8. Examples of noisy images of slow-vehicle ahead sign at three different poses in an uncluttered environment.

the target, the Lipschitz constant  $L_{\triangleright}$  can be controlled during the training of the encoder using regularization and smoothing techniques.

2) The maximum test error  $\epsilon$  which reflects the quality of the encoder's training.

#### D. Encoder Robustness to Image Noise

We now extend the results of Theorem 1 to account for images with bounded pixel-wise noise.

**Definition 10** (Bounded Pixel Noise). *An image  $\tilde{I}_{\xi}$  is said to have bounded pixel noise if:*

$$\|\tilde{I}_{\xi} - I_{\xi}\| \leq \bar{n},$$

where  $I_{\xi}$  is the ideal image of the target object at pose  $\xi$ , and  $\bar{n} > 0$  is the maximum noise level.

The definition above captures various types of noise that may affect at most  $n = \bar{n}^2$  pixels in the image. Fig. 8 shows an example of a noisy image with bounded pixel noise. We now establish the certifiable performance of the encoder  $\mathcal{NN}_{\triangleright}$  when applied to images with bounded pixel noise.

**Corollary 1** (Estimation Error Bounds under Bounded Noise). *Consider a system  $(\mathcal{T}, \bar{\mathcal{T}}, \mathcal{C}_{\mathcal{T}}, \Xi)$  where  $\bar{\mathcal{T}} = \emptyset$ , i.e., an uncluttered environment. Assume that the encoder  $\mathcal{NN}_{\triangleright}$  is trained using Algorithm 1, then, for any noisy image  $\tilde{I}_{\xi}$  with bounded pixel noise  $\bar{n} > 0$ , the following bound on the pose estimation error holds:*

$$\max_{\xi \in \Xi_{\mathcal{T}}} \|\xi - \mathcal{NN}_{\triangleright}(\tilde{I}_{\xi})\| \leq (\delta + \eta) (L_{\triangleleft} L_{\triangleright} + 1) + L_{\triangleright} \bar{n} + \epsilon.$$

The proof of Corollary 1 follows the same structure as that of Theorem 1, with the addition of a term accounting for the noise in the input image.

## V. CERTIFIED VISION-BASED OBJECT DETECTION FOR UNCLUTTERED ENVIRONMENTS

#### A. Problem Overview

In the previous section, we addressed the pose estimation problem under the assumption that the target object is present in the captured image. In this section, we relax this assumption and consider the object detection problem: given an image, the goal is to determine whether the target object is present in the scene. Effectively, the object detection problem serves as a prerequisite to the pose estimation framework.

**Problem 4** (Object Detection). *Consider a system  $(\mathcal{T}, \bar{\mathcal{T}}, \mathcal{C}_{\mathcal{T}}, \Xi_{\mathcal{T}})$  where  $\bar{\mathcal{T}} = \emptyset$ . Given an image  $I \in \mathcal{I}$*

*captured by the camera  $\mathcal{C}_{\mathcal{T}}$  at unknown pose  $\xi \in \Xi_{\mathcal{T}}$ , design a detector  $\mathcal{NN}_{\exists} : \mathcal{I} \rightarrow \{\top, \perp\}$  such that:*

$$\mathcal{NN}_{\exists}(I) = \begin{cases} \top & \text{if } \exists \xi \in \Xi_{\mathcal{T}} \text{ s.t. } I = \mathcal{C}_{\mathcal{T}}(\xi), \\ \perp & \text{otherwise.} \end{cases}$$

A straight forward approach to solve Problem 4 is to check if the image  $I$  belongs to the forward reachable set  $\mathcal{R}(\mathcal{NN}_{\triangleleft}, \Xi)$  of the GGM-based decoder where  $\mathcal{R}(\mathcal{NN}_{\triangleleft}, \Xi)$  is defined as:

$$\mathcal{R}(\mathcal{NN}_{\triangleleft}, \Xi) = \{I \in \mathcal{I} \mid \exists \xi \in \Xi. I = \mathcal{NN}_{\triangleleft}(\xi)\}.$$

Unfortunately, computing the exact forward reachable set of deep neural networks is computationally intractable [3], [30], [31] and current techniques rely on coarse over-approximation of such sets [20], [32]–[34]. To that end, we first present a lightweight and accurate technique that exploits the properties of the GGM-based decoder network followed by our approach to solve Problem 4.

#### B. Computing Reachable Set of GGM-Based Detectors Using Grid Sampling

Given a compact set  $\Xi \subset \mathbb{R}^6$ , we construct a sampling grid with step size  $h$  that satisfies  $h < L_{\triangleleft}^{-1}$ , where  $L_{\triangleleft}^{-1}$  is the Lipschitz constant of the GGM decoder network. The output of this step is a discrete set of candidate poses  $\Xi_d$ . For each candidate pose  $\xi_i \in \Xi_d$ , we apply the decoder  $\mathcal{NN}_{\triangleleft}$  to generate the corresponding image:

$$I_i = \mathcal{NN}_{\triangleleft}(\xi_i).$$

The reachable set  $\mathcal{R}(\mathcal{NN}_{\triangleleft}, \Xi)$  is then computed by taking the union over all the generated images  $I_i$ . This process is summarized in Algorithm 2.

The condition  $h < L_{\triangleleft}^{-1}$  is critical for correctness of Algorithm 2. As shown later in the proof of Theorem 2, this condition combined with the grid resolution, ensures to find all poses that produce images that differ strictly by less than 1 pixel. In other words, this approach exploits the fact that the GGM networks imposes a partitioning of the  $\Xi$  set into a set of equivalent classes (due to the digital behavior of the GGM), where each equivalent class of poses generate the same exact image. The grid sampling approach above is then guaranteed to cover all possible equivalent classes and hence transforms the problem of computing a reachable set over the continuous space  $\Xi$  into an equivalent one over the discrete set  $\Xi_d$ .

#### C. GGM-Based Object Detection Framework

Now, we address Problem 4 by leveraging the pose estimation framework developed in Section IV along with the forward reachability approach in Algorithm 2. The proposed detection pipeline is illustrated in Fig. 9. Consider a pose space  $\Xi_{\mathcal{T}} \subset \mathbb{R}^6$  and suppose an image  $I$  is captured by the camera at some unknown pose  $\xi \in \Xi_{\mathcal{T}}$ . Given that both the camera parameters and the target object geometry are known a priori, we can use the pose estimation framework to design a certifiable pose estimator  $\mathcal{NN}_{\triangleright}$  for  $\mathcal{T}$  using Algorithm 1.

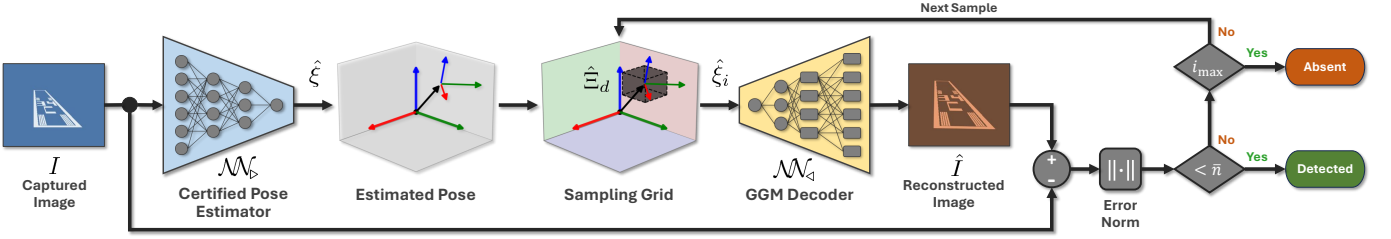


Fig. 9. GGM-based object detection framework. Given an input image  $I$  captured at unknown pose, a certified pose estimator  $\mathcal{N}_\triangleright$  is used first to estimate the pose  $\hat{\xi}$ , which is then used to construct a sampling grid over the certified error bound set  $\hat{\Xi}$ . The GGM decoder  $\mathcal{N}_\triangleleft$  is then applied to each sampled pose in the grid to generate the corresponding images, which are compared with  $I$  to determine whether the target object is present in the scene.

---

**Algorithm 2:** Forward reachability via grid sampling

---

**Input:**  $\Xi \subset \mathbb{R}^6$ , compact pose space;  
 $\mathcal{N}_\triangleleft$ , a GGM-based decoder;  
**Output:**  $\Xi_d$ , discrete set of sampled poses;  
 $\mathcal{R}$ , the forward reachable set of  $\mathcal{N}_\triangleleft$ ;

```

1 function FWDReach-GridSampling( $\Xi, h$ ):
2    $\Xi_d \leftarrow \emptyset$ ;  $\mathcal{R} \leftarrow \emptyset$ ;
3    $\underline{\xi} \leftarrow \inf \Xi$ ;  $\bar{\xi} \leftarrow \sup \Xi$ ;
4    $h \leftarrow L_\triangleleft^{-1} - \mathbf{c}$ ; // for any small constant  $\mathbf{c} > 0$ .
5   foreach  $k \in \mathbb{Z}^6$  s.t.  $\underline{\xi}_i + k_i h \leq \bar{\xi}_i$ ,  $i = 1, \dots, 6$  do
6      $\xi \leftarrow \underline{\xi} + k \odot h$ ;
7      $\Xi_d \leftarrow \Xi_d \cup \{\xi\}$ ;
8      $\mathcal{R} \leftarrow \mathcal{R} \cup \{\mathcal{N}_\triangleleft(\xi)\}$ 
9   return  $(\Xi_d, \mathcal{R})$ 

```

---

As detailed in Algorithm 3, the detection procedure operates as follows. First, we apply the certified pose estimator  $\mathcal{N}_\triangleright$  to the input image  $I$  to obtain an initial pose estimate:

$$\hat{\xi} = \mathcal{N}_\triangleright(I).$$

Recall from Theorem 1 that the error bounds certified for  $\mathcal{N}_\triangleright$  guarantee that if  $\xi \in \Xi_\mathcal{T}$ , then  $\|\xi - \hat{\xi}\| \leq r$ , where  $r := (\delta + \eta)(L_\triangleleft L_\triangleright + 1) + \epsilon$  is the certified error radius.

To verify whether the target is present in the image, we construct the forward reachable set  $\mathcal{R}(\mathcal{N}_\triangleleft, \hat{\Xi})$  where:  $\hat{\Xi} = \{\xi \in \Xi_\mathcal{T} \mid \|\xi - \hat{\xi}\| \leq r\}$ . We then compute the distance between the original image  $I$  and the images in the forward reachable set  $I_i$ :

$$d_i = \|I - I_{\xi_i}\| \quad \forall I_{\xi_i} \in \mathcal{R}(\mathcal{N}_\triangleleft, \hat{\Xi}).$$

If there exists any candidate pose  $\xi_i$  such that  $d_i = 0$  (i.e., the generated image matches the input image exactly), we conclude that the target object is present in the scene. Otherwise, the target is absent. The complete procedure is summarized in Algorithm 3.

#### D. Correctness Analysis

We now provide a formal proof of the correctness of our GGM-based detection framework as follows.

**Theorem 2** (Correctness of Object Detection). *Let  $\mathcal{N}_\triangleleft : \Xi_\mathcal{T} \rightarrow \mathcal{I}$  be a GGM-based decoder that satisfies Assumption 1 with Lipschitz constant  $L_\triangleleft$ , and let  $\mathcal{N}_\triangleright : \mathcal{I} \rightarrow \Xi_\mathcal{T}$  be a certified pose estimator satisfying the error bound of Theorem 1.*

---

**Algorithm 3:** GGM-Based Object Detection

---

**Input:**  $I$ , captured image;  
 $\Xi_\mathcal{T}$ , target pose space region;  
**Output:** isDetected, detection status  
 $\hat{\xi}$ , estimated pose

```

1 function  $\mathcal{N}_\exists(I, \Xi_\mathcal{T})$ :
2    $\hat{\xi} \leftarrow \mathcal{N}_\triangleright(I)$  ;
   // Apply certified pose estimator to full pose space
3    $r \leftarrow (\delta + \eta)(L_\triangleleft L_\triangleright + 1) + \epsilon$  ;
   // Compute certified error radius
4    $\hat{\Xi} = \{\xi \in \Xi_\mathcal{T} \mid \|\xi - \hat{\xi}\| \leq r\}$ ;
5    $(\Xi_d, \mathcal{R}) \leftarrow \text{FWDReach-GridSampling}(\hat{\Xi}, \mathcal{N}_\triangleleft)$ ;
6   foreach  $(\xi_i, I_{\xi_i}) \in (\Xi_d, \mathcal{R})$  do
7     if  $\|I_{\xi_i} - I\| \leq \tau$  then
8       return  $(\top, \hat{\xi})$ ; // Target present
9   return  $(\perp, \emptyset)$ ; // Samples exhausted, target absent

```

---

If the grid sampling step size used to compute the forward reachable set  $\mathcal{R}(\mathcal{N}_\triangleleft, \hat{\Xi})$  satisfies  $h < L_\triangleleft^{-1}$ , then Algorithm 3 (with  $\tau = 0$ ) is correct in the following sense:

- Soundness:** If  $\mathcal{N}_\exists(I, \Xi_\mathcal{T}) = \top$ , then  $\xi \in \Xi_\mathcal{T}$  (the target is present).
- Completeness:** If  $\xi \in \Xi_\mathcal{T}$  and  $I = \mathcal{N}_\triangleleft(\xi)$ , then  $\mathcal{N}_\exists(I, \Xi_\mathcal{T}) = \top$  (the target will be detected).

*Proof.* We prove each property separately.

a) **Soundness:** This follows directly by construction. If the algorithm returns  $\top$  at Line 8, then there exists some  $\xi_i \in \Xi_d$  such that  $\|\mathcal{N}_\triangleleft(\xi_i) - I\| \leq \tau$ . Since  $\Xi_d \subseteq \Xi_\mathcal{T}$  by construction, we conclude that the target is present.

b) **Completeness:** Assume for the sake of contradiction that the target is present, i.e.,  $I = \mathcal{N}_\triangleleft(\xi)$  for some true (unknown) pose  $\xi \in \Xi_\mathcal{T}$ , yet the algorithm returns  $\perp$  (i.e., claims the target is absent). Since  $\perp$  was returned, then all grid points in  $\Xi_d$  are exhausted without finding a match. That is,  $\forall \hat{\xi}_i \in \Xi_d$  we have:

$$\|\mathcal{N}_\triangleleft(\hat{\xi}_i) - I\| > \tau. \quad (15)$$

Now, by Theorem 1, and since  $I = \mathcal{N}_\triangleleft(\xi)$  is a clean image of the target at pose  $\xi$ , the encoder estimate  $\hat{\xi} = \mathcal{N}_\triangleright(I)$  satisfies the following bound:

$$\|\xi - \hat{\xi}\| \leq r = (\delta + \eta)(L_\triangleleft L_\triangleright + 1) + \epsilon.$$

This means that  $\xi$  lies within the certified error ball of radius  $r$  centered at  $\hat{\xi}$ . By the construction of the grid sampling in Algorithm 2, which discretizes this ball with step size  $h$ , there exists some grid point  $\xi_j \in \Xi_d$  such that:

$$\|\xi - \xi_j\| \leq h. \quad (16)$$

Now we apply the Lipschitz continuity of the decoder  $\mathcal{NN}_d$ . Since  $\mathcal{NN}_d$  has Lipschitz constant  $L_d$ , we have:

$$\|\mathcal{NN}_d(\xi) - \mathcal{NN}_d(\xi_j)\| \leq L_d \|\xi - \xi_j\| \quad (17)$$

$$\leq L_d \cdot h \quad (\text{by (16)})$$

$$< 1 \quad (\text{by definition of } h). \quad (18)$$

Let  $I_{\xi_j} = \mathcal{NN}_d(\xi_j)$  denote the image generated at the grid point  $\xi_j$ . From (18), we have:

$$\|I - I_{\xi_j}\| < 1.$$

Since fewer than 1 pixel can differ, the two images are identical. Therefore, at  $\xi_j$ , we have:

$$\|\mathcal{NN}_d(\xi_j) - I\| = 0 \leq \tau,$$

which means Line 8 of Algorithm 3 should have returned  $\top$ . This contradicts our assumption in (15) that all grid points failed the detection test. Therefore, if the target is present (i.e.,  $I = \mathcal{NN}_d(\xi)$  for some  $\xi \in \Xi_{\mathcal{T}}$ ), the algorithm must return  $\top$ , establishing its completeness.  $\square$

The theorem can also be extended to handle noisy images by replacing the detection threshold  $\tau = 0$  with  $\tau = \bar{n}$ , where  $\bar{n}$  is the noise budget as defined in Corollary 1. In this case, the bound in (18) becomes:

$$\|I - I_{\xi_j}\| \leq L_d \cdot h + n < 1 + n. \quad (19)$$

If  $\tau \geq L_d \cdot h + n$ , the algorithm remains correct up to the specified noise margin.

## VI. CERTIFIED VISION-BASED FILTERING AND POSE ESTIMATION FOR CLUTTERED ENVIRONMENTS

This section addresses the problem of pose estimation in cluttered environments, where multiple objects may be present in the captured image and the presence of the target object is not known a priori. Fig. 10 illustrates an example of such a scenario, where the target object is surrounded by various clutter objects. The objective is to design an algorithm that determines whether the target object is present and, if so, estimates the camera pose relative to it. This extends the earlier assumption of uncluttered environments, in which the image may only contain the target object. In that case, a GGM-based detector was used to verify target presence (see Section V) and, upon detection, to estimate the camera pose relative to the target.

**Problem 5** (Pose Estimation in Cluttered Environments). Consider a system  $(\mathcal{T}, \bar{\mathcal{T}}, \mathcal{C}, \Xi_{\mathcal{T}})$ , where  $\bar{\mathcal{T}}$  denotes a possibly nonempty set of clutter objects. Let  $\Xi_{\mathcal{T}} \subset \Xi$  denote the subset of poses for which the target object  $\mathcal{T}$  is present in the scene.



Fig. 10. Example of a cluttered environment where the target object (the runway) is surrounded by various clutter objects.

Given an image  $I \in \mathcal{I}$  captured by the camera  $\mathcal{C}_{\mathcal{T}}$  at unknown pose  $\xi \in \Xi$ , design a detector:

$$\mathcal{NN}_{\Xi}^c: \mathcal{I} \rightarrow \{\top, \perp\} \times (\Xi_{\mathcal{T}} \cup \{\emptyset\}),$$

such that:

$$\mathcal{NN}_{\Xi}^c(I) = \begin{cases} (\top, \hat{\xi}) & \text{if } \xi \in \Xi_{\mathcal{T}}, \\ (\perp, \emptyset) & \text{otherwise,} \end{cases}$$

$$\max_{\xi \in \Xi_{\mathcal{T}}} \|\xi - \hat{\xi}\| \leq \epsilon_{\text{bound}} \quad \text{if } \xi \in \Xi_{\mathcal{T}},$$

where  $\hat{\xi} \in \Xi_{\mathcal{T}}$  is the estimated pose of the camera.

### A. Spatial Filtering for Clutter Removal

The key challenge in cluttered environments is that the object detector (see Section V) assumes that the target object is the only object present in the image. In cluttered scenes, the object is surrounded by clutter, which interferes with the detection process. We address Problem 5 by proposing a spatial filtering approach where we partition the pose space into regions, design a specialized detector for each region, and combine their outputs. Consider a bounded pose space  $\Xi_{\mathcal{T}} \subset \Xi$ . We partition  $\Xi_{\mathcal{T}}$  into a  $K$  non-overlapping partitions  $\{\Xi_1, \dots, \Xi_K\}$  such that:

$$\bigcup_{i=1}^K \Xi_i = \Xi_{\mathcal{T}} \quad (20)$$

$$I' \odot \bigvee_{I \in \mathcal{R}(\Xi_i, \mathcal{NN}_d)} I \notin \mathcal{R}(\Xi_i, \mathcal{NN}_d) \quad \text{for all } I' \in \Xi_j \text{ with } j \in \{1, \dots, K\} \setminus \{i\}, \quad (21)$$

where  $\bigvee$  denotes the pixel-wise logical OR operation and  $\odot$  denotes the pixel-wise logical AND operation. For each hypercube  $\Xi_i$ , we construct a spatial filter  $H_i$  that isolates the portion of an image corresponding to all poses  $\xi \in \Xi_i$ . Through the forward reachability analysis discussed in Algorithm 2, the spatial filter  $H_i$  is realized as the binary mask:

$$M_i = \bigvee_{\xi \in \Xi_i} \mathcal{NN}_d(\xi) = \bigvee_{I \in \mathcal{R}(\Xi_i, \mathcal{NN}_d)} I. \quad (22)$$

That is, the mask  $M_i$  represents the union of all images that can be generated by  $\mathcal{NN}_d$  for poses in  $\Xi_i$ . Applying the spatial filter  $H_i$  to an image  $I$  results in the filtered image:

$$\tilde{I}_i = H_i(I) = I \odot M_i.$$

**Algorithm 4:** Spatial Filter Mask Construction

**Input:**  $\Xi_i$  (pose space region);  
 $\mathcal{NN}_\triangleleft$  (GGM decoder);  
**Output:**  $M_i$  (spatial filter mask)

```

1 Initialize  $M_i \leftarrow \mathbf{0}^{h \times w}$ ;  

2 Construct the forward reachable set  

 $(-, \mathcal{R}_i) \leftarrow \text{FWDReach-GridSampling}(\Xi_i, \mathcal{NN}_\triangleleft)$ ;  

3 foreach  $I \in \mathcal{R}_i$  do  

4    $M_i \leftarrow M_i \vee I$  ; // Accumulate via logical OR  

5 return  $M_i$ ;
```

Algorithm 4 outlines the procedure for constructing the spatial filter mask  $M_i$  for a given pose space partition  $\Xi_i$ . Since  $\Xi_i$  is a continuous set, it cannot be directly used to construct the mask. Therefore, we start by constructing the forward reachable set  $\mathcal{R}(\Xi_i, \mathcal{NN}_\triangleleft)$  to find all possible images that can be generated within  $\Xi_i$ . The mask  $M_i$  is then constructed by accumulating the logical OR of all generated images. Due to the choice of the grid sampling step size  $h$  in Algorithm 2, the algorithm ensures that all possible images generated by poses in  $\Xi_i$  are captured in the mask  $M_i$ .

### B. Correctness of Spatial Filtering

We now establish the correctness properties of the spatial filtering mechanism described earlier. The correctness relies on two fundamental properties: preservation and exclusion. The preservation property ensures that if the true pose  $\xi$  lies within a partition  $\Xi_i$ , the spatial filter retains the target object in the filtered image. The exclusion property ensures that if the true pose lies outside all partitions, the spatial filter removes the target object from all filtered images.

**Lemma 1** (Spatial Filter Preservation). *Let  $\Xi_i$  be a pose space partition—that satisfies Assumption 1—and  $M_i$  be the corresponding spatial filter mask constructed by Algorithm 4. For any pose  $\xi \in \Xi_i$ , the filtered image satisfies:*

$$\mathcal{NN}_\exists(H_i(I_\xi), \Xi_i) = \mathcal{NN}_\exists(I_\xi \odot M_i, \Xi_i) = \top.$$

where  $I_\xi = \mathcal{NN}_\triangleleft(\xi)$  is the ideal image of the target at pose  $\xi$ .

*Proof.* By construction, the mask  $M_i$  is the logical OR of all images in  $\mathcal{I}_i = \mathcal{R}(\mathcal{NN}_\triangleleft, \Xi_i)$ . Since  $\xi \in \Xi_i$ , it follows that  $I_\xi \in \mathcal{I}_i$ . Therefore,  $I_\xi$  is included in the logical OR operation that defines  $M_i$ , which implies that for every pixel where  $I_\xi$  has value 1, the mask  $M_i$  also has value 1. Consequently,  $I_\xi \odot M_i = I_\xi$ . The result then follows directly from Theorem 2 since  $I_\xi \in \Xi_i$ .  $\square$

**Lemma 2** (Spatial Filter Exclusion). *Let  $\Xi_i$  be a pose space partition—that satisfies Assumption 1—and a corresponding spatial filter mask  $M_i$ . For any pose  $\xi \notin \Xi_i$ , the filtered image satisfies:*

$$\mathcal{NN}_\exists(H_i(I_\xi), \Xi_i) = \mathcal{NN}_\exists(I_\xi \odot M_i, \Xi_i) = \perp.$$

*Proof.* We prove this by contradiction. Assume that  $\xi \notin \Xi_i$  but  $\mathcal{NN}_\exists(H_i(I_\xi), \Xi_i) = \top$ . It follows from Theorem 2 that this equality implies that  $H_i(I_\xi) \in \mathcal{R}(\Xi_i, \mathcal{NN}_\triangleleft)$  which contradicts the condition in (21).  $\square$

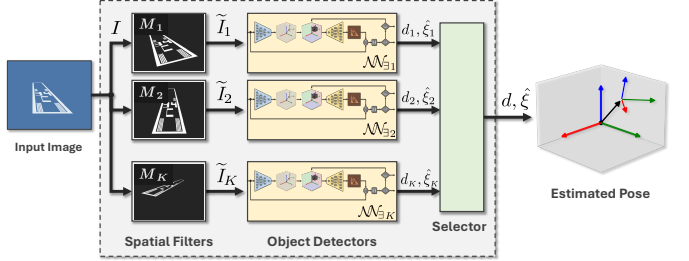


Fig. 11. GGM-based spatial filtering pipeline for certified pose estimation in cluttered environments. An input image from a cluttered environment is processed by multiple spatial filters, each corresponding to a partition of the pose space. Each filtered image is then analyzed by a certified object detector. The outputs of the detectors are combined through a selection process that minimizes residual clutter, yielding the final pose estimate.

**Algorithm 5:** Certified Pose Estimation in Cluttered Environments

**Input:**  $I$  (input image),  $\{M_1, \dots, M_K\}$  (spatial filter masks),  $\mathcal{NN}_\exists$  (certified detector),  $\mathcal{NN}_\triangleleft$  (GGM decoder),  $\epsilon_{\text{bound}}$  (certified error bound)

**Output:**  $(d, \hat{\xi})$  (detection status and estimated pose)

```

1  $\mathcal{H} \leftarrow \emptyset$  ; // Detection set
2 for  $i = 1$  to  $K$  do
3    $\tilde{I}_i \leftarrow I \odot M_i$  ; // (1) Spatial filtering
4    $(d_i, \hat{\xi}_i) \leftarrow \mathcal{NN}_\exists(\tilde{I}_i)$  ; // (2) Certified detection
5    $\mathcal{H} \leftarrow \mathcal{H} \cup \{\hat{\xi}_i\}$ ;
6  $\bar{\mathcal{H}} \leftarrow \text{User-Specified-Criteria}(\mathcal{H})$  ; // (3) Selection
7 return  $\bar{\mathcal{H}}$ ;
```

### C. Certified Pose Estimation in Cluttered Environments

As illustrated in Fig. 11, our approach for pose estimation in cluttered environments integrates the spatial filtering mechanism with certified object detection to produce reliable detection and pose estimates. The pipeline comprises three sequential stages: spatial filtering, certified detection, and selection. In the first stage, the input image  $I$  is processed by  $K$  spatial filters  $\{H_1, \dots, H_K\}$ , each corresponding to a partition  $\Xi_i$  of the target pose space. Each spatial filter applies its mask  $M_i$  to the input image, yielding the filtered image  $\tilde{I}_i = I \odot M_i$ . This operation isolates the portion of the image that could correspond to the target object at poses within  $\Xi_i$ , while suppressing clutter from other regions. In the second stage, each filtered image  $\tilde{I}_i$  is analyzed by its certified object detector  $\mathcal{NN}_\exists$  that corresponds to the pose space partition  $\Xi_i$  (see Algorithm 3).

For each filtered image, the detector either signals the absence of the target object ( $d_i = \perp$ ) or provides a pose estimate  $\hat{\xi}_i$  with detection status  $d_i = \top$ . The set of all detections is collected in  $\mathcal{H}$ . Since multiple objects might exist in the scene, the algorithm then returns  $(\perp, \emptyset)$  if no detections were made, or the entire set  $\mathcal{H}$  otherwise. A third (optional) stage, is a selection mechanism that picks all of a subset of the set  $\mathcal{H}$  depending on user specific criteria (e.g., closest detected object). The complete pipeline is formalized in Algorithm 5.

However, the correctness of this localized detection pipeline

relies on the purity of the filtered image  $\tilde{I}_{i^*} = I \odot M_{i^*}$  for the partition  $i^*$  where the unknown pose belongs to. If the spatial filter  $M_{i^*}$  captures significant portions of the background clutter alongside the object, the resulting signal may breach the detector  $\mathcal{NN}_\exists$  decision threshold  $\tau$ .

Therefore, to guarantee valid pose estimation and object detection, we must constrain the spatial relationship between the target object  $\mathcal{T}$  and environmental clutter  $\bar{\mathcal{T}}$ . We introduce a Clutter Intrusion Bound. This condition posits that either the scene layout provides sufficient physical clearance to spatially isolate the object, or, if overlap occurs, the magnitude of the clutter’s contribution to the filtered image  $I \odot M_{i^*}$  remains below the noise level  $\bar{n}$  used to tune the detection threshold  $\tau$ . This duality allows us to trade off spatial constraints (requiring clear backgrounds) with detector robustness (tolerating minor occlusions or background noise), providing a flexible theoretical basis for deployment.

**Assumption 2** (Bounded Clutter Intrusion). *Consider a bounded pose space  $\Xi_{\mathcal{T}} \subset \Xi$  and a non-overlapping partitioning  $\{\Xi_1, \dots, \Xi_K\}$  that satisfies (20)-(21). Let  $\Xi_{i^*}$  denote the partition for which the unknown pose  $\xi$  belongs, i.e.,  $\xi \in \Xi_{i^*}$ . Let  $\bar{n}$  be the noise threshold used to tune the detection threshold  $\tau$  used by  $\mathcal{NN}_\exists$ . We assume that  $\bar{n}$  is selected such that  $\|I_{\bar{\mathcal{T}}} \odot M_{i^*}\| \leq \bar{n}$ .*

This inequality consolidates two distinct operating regimes into a single constraint:

- 1) **Spatial Isolation** ( $\bar{n} = 0$ ): The target object  $\mathcal{T}$  is sufficiently separated from clutter such that the filter  $M_{i^*}$  effectively excludes all clutter pixels. This corresponds to a minimum spatial clearance that depends on the volume of  $\Xi_{i^*}$ .
- 2) **Robust Detection** ( $\bar{n} > 0$ ): Clutter partially intrudes into the filter window, but its magnitude is suppressed by the detector’s inherent noise rejection threshold  $\tau$ .

**Theorem 3** (Pipeline Correctness). *Consider a pose space  $\Xi_{\mathcal{T}}$  that satisfies Assumption 1 and a partitioning  $\{\Xi_1, \dots, \Xi_K\}$  that satisfies (20)-(21). Let  $\Xi_{i^*}$  denote the partition for which the unknown pose  $\xi$  belongs, i.e.,  $\xi \in \Xi_{i^*}$ . For a cluttered image  $I_\xi$  captured at unknown pose  $\xi \in \Xi_{\mathcal{T}}$ , and under the Bounded Clutter Intrusion assumption (Assumption 2), the pipeline in Algorithm 5 satisfies:*

- 1) **Uniqueness under Spatial Isolation:** *If the spatial filter  $M_{i^*}$  achieves perfect spatial isolation (i.e.,  $\bar{n} = 0$ ), the algorithm returns a unique valid pose, i.e.:*

$$\mathcal{H} = \{\hat{\xi}^*\} \text{ and } \|\xi - \hat{\xi}^*\| \leq (\delta + \eta)(L_{\triangleleft} L_{\triangleright} + 1) + \epsilon. \quad (23)$$

- 2) **Validity under Robust Detection:** *If the clutter intrusion in  $M_{i^*}$  is non-zero but bounded ( $\bar{n} > 0$ ), the algorithm returns a candidate set  $\mathcal{H}$  that is guaranteed to include the ground truth, i.e.:*

$$|\mathcal{H}| \geq 1 \text{ and } \exists \hat{\xi}^* \in \mathcal{H} \text{ such that:}$$

$$\|\xi - \hat{\xi}^*\| \leq (\delta + \eta)(L_{\triangleleft} L_{\triangleright} + 1) + L_{\triangleright} \bar{n} + \epsilon. \quad (24)$$

In other words, Theorem 3 distinguishes the behavior of Algorithm 5 under these two operating regimes by analyzing

the cardinality of the solution set  $\mathcal{H}$ . In the Spatial Isolation regime, where the filter  $M_{i^*}$  successfully excludes all external clutter, the filtered image  $I \odot M_{i^*}$  conforms strictly to the generative model of the object. Consequently, the inverse map converges to a unique solution, returning a singleton set containing the optimal pose estimate. Conversely, in the Robust Detection regime, the intrusion of clutter—even within the permissible bound—may introduce ambiguity. Under these conditions, our algorithm generalizes to a set-valued estimator, returning a discrete set of candidate poses. While the presence of clutter prevents us from guaranteeing uniqueness (cardinality of one), the calibration of the bound  $\tau$  ensures validity: the set of candidates is guaranteed to contain the ground truth pose.

*Proof.* We start by proving (24). It follows from (20) that there exists some  $i^*$  such that  $\xi \in \Xi_{i^*}$ . By Lemma 1 and Assumption 2, the certified detector from Algorithm 3 correctly detects the target object in  $I_\xi \odot M_{i^*}$ , it returns  $d_{i^*} = \top$  for  $\tilde{I}_{i^*}$ . Therefore, the algorithm adds  $d_{i^*} = \top$  and  $\hat{\xi}_{i^*}$  to  $\mathcal{H}$ .

The uniqueness of solutions in (23), follows from Assumption 2 and Lemma 2 where all partitions other than  $i^*$  will be rejected by the detector  $\mathcal{NN}_\exists$ .  $\square$

## VII. EVALUATION

In this section, we present a series of experiments to evaluate various aspects of the proposed framework. In Experiment 1, we evaluate the correctness of the GGM computational graph detailed in Fig. 6 using two examples: a stop sign and runway markings. Experiment 2 validates the certified pose estimation algorithm (Algorithm 1) and the theoretical error bounds established in Theorem 1 in uncluttered environments. Finally, Experiment 3 assesses the performance of the detection and pose estimation pipeline in cluttered environments (Algorithm 5).

### A. Experimental Setup

For the experiments, we implemented the GGM computational graph in Python using PyTorch. The experiments were conducted on an Apple M1 Pro processor with 32 GB of RAM. Experiments 1 and 2 used synthetic images, while Experiment 3 used real images captured by a SilkyEvCam event-based camera with known intrinsic parameters ( $w = 640$ ,  $h = 480$ ,  $f = 8$  mm, pixel size  $15 \mu\text{m} \times 15 \mu\text{m}$ ). In the latter case, the ground truth of the camera pose was measured using a Vicon motion capture system.

Overall, three target objects were considered in the experiments. The first target is a stop sign of size 0.75 m in length and 0.75 m in width (see Fig. 3). The target object was modeled as a composition of 12 polygons, composed together using a mix of union and difference operations. For instance, the octagonal shape of the stop sign involves two polygons: an outer octagon  $V_{\text{outer}}$  and an inner octagon  $V_{\text{inner}}$ , comprising 8 vertices each, and composed together using the expression  $V_{\text{outer}} \oplus V_{\text{inner}}$  (see Table I). Similarly, the letter “T” in “STOP” is modeled as the union of its two constituent rectangles.

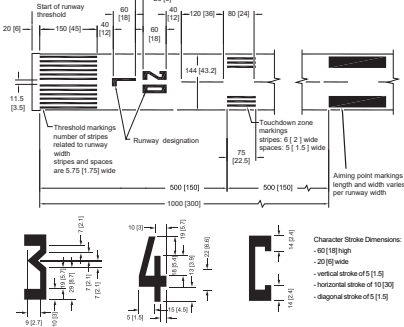


Fig. 12. Standard dimensions of runway markings (in meters [feet]) [2] used to design the runway GGM. The runway is 300 m in length and 60 m in width, and starts with threshold markings, followed by one letter and two digits indicating the runway's identifier.

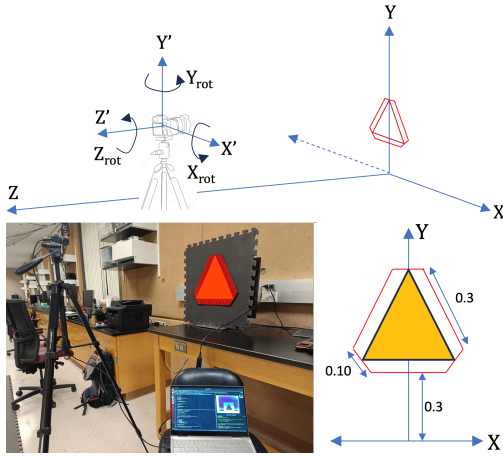


Fig. 13. Experimental setup for the slow-vehicle ahead sign. The SilkyEvCam event-based camera is fixed in position, and the slow-vehicle ahead sign is placed on the XY plane. The relative pose between the camera and the sign is defined by the coordinates  $(x, y, z)$  and the angles  $(\theta, \phi, \psi)$ .

The second target object is an airport runway markings, scaled down to 0.3 m in length and 0.1 m in width. As shown in Fig. 12, the runway markings consist of a series of white stripes indicating its threshold for landing, and one character and two digits indicating the runway's identifier. These standard runway markings [2] are used to provide visual aids for aircrafts during landing. The runway is modeled as a composition of polygons and the GGM is designed following the same process. Finally, a physical slow-vehicle ahead sign of size 14 in  $\times$  16 in is used. As shown in Fig. 13, the sign is placed on a planar surface, and images are captured using the event-based camera at various relative poses between the camera and the sign.

The process for designing a GGM is illustrated in Fig. 14. First, an XML file is used to specify the target object's geometry: vertices are specified as 2D coordinates (in the TCF) using `<point>` elements, and polygons are defined as sets of vertices using `<polygon>` elements. Note that 2D coordinates suffice for defining vertices since the target is a planar object on the XY plane. The expression used to specify how to compose the polygons to form the target object is given in the `<composition>` element. In turn, the XML is used to configure the parameters of the GGM computational graph

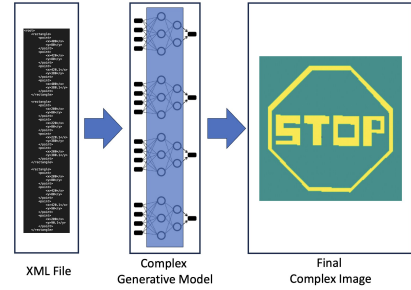


Fig. 14. Streamlines process for designing the GGM of a target object. The object's geometry and the camera intrinsic parameters are both specified in an XML file and used to configure the GGM.

TABLE III. Comparison of the target complexity and number of nodes per layer of each of the three GGMs, designed for image sizes of 640  $\times$  480 pixels.

Target	Polygons	Vertices	L0	L1	L2	L3	L4
Stop Sign	13	58	116	17,817,600	36,249,600	614,400	307,200
Runway Markings	16	64	128	19,660,800	39,936,000	614,400	307,200
Slow-Vehicle Sign	3	12	24	3,686,400	7,987,200	614,400	307,200

in Fig. 6. The result is a decoder that takes the camera pose as input and generates the image of the target object.

### B. Experiment 1: Evaluating the GGM Correctness

In this experiment, we assess the correctness of the GGM by comparing the generated images with the ground truth images captured by the event-based camera. Following the process described earlier, GGMs were designed for the three target objects at a pixel resolution (640  $\times$  480p) that matches the camera's resolution. Fig. 15 shows examples of the images generated by each GGM at different camera poses. Table III compares the sizes and complexities of the three GGMs designed. The runway GGM is the largest and most complex among the three, as it represents a larger target object with more intricate details. The impact of image resolution is evaluated in Fig. 15(c), which shows the images generated by three different GGMs of the same target but with different output resolutions: high (640  $\times$  480p), medium (120  $\times$  100p), and low (60  $\times$  30p).

We also compare the images generated by the HighRes GGM of the slow-vehicle ahead sign with the images captured by the actual camera at different poses as shown in Fig. 16. We observe that the GGM-generated images closely resemble the camera images. Moreover, the three resolutions of the GGM images demonstrate that the GGM can generate images at different qualities while maintaining the same target location and orientation within the image. The maximum distance between each vertex in the GGM and its corresponding pixel in the generated image is approximately 3 pixels for the high-resolution image, and decreases to less than 1 pixel for the low-resolution image.

### C. Experiment 2: Certifying the Error Bounds of the Pose Estimator

We evaluate the error bounds of the pose estimation framework in Section IV, the slow-vehicle ahead sign was used as

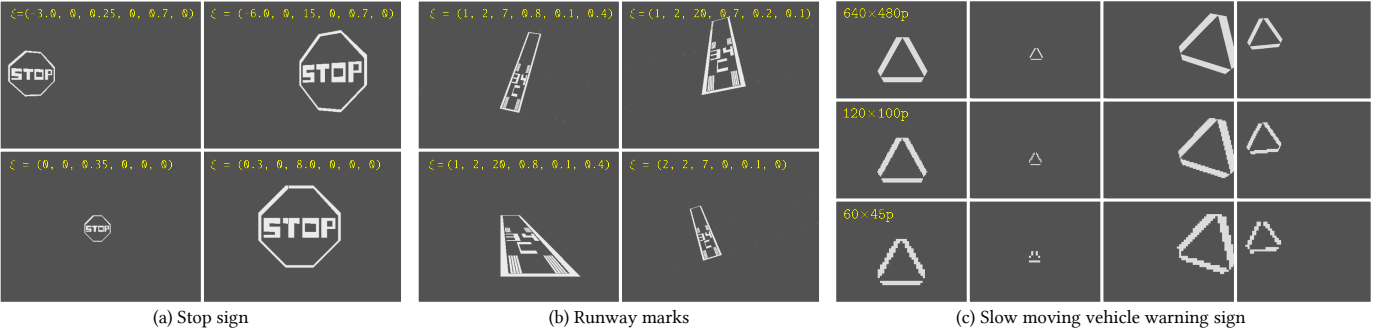


Fig. 15. Images generated for three different planar objects using their respective GGMs, with four different camera poses each. In (c), a comparison between images of the slow-vehicle ahead sign at three different resolutions is shown.

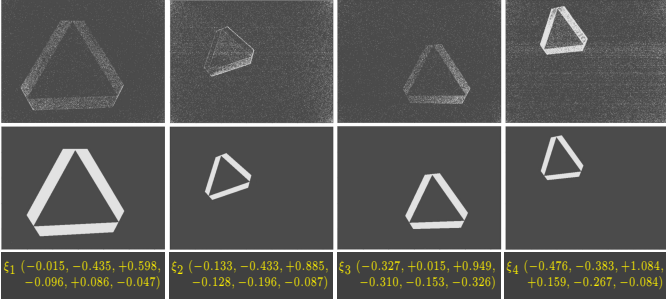


Fig. 16. Camera(Top) vs GGM(Bottom) for High Resolution Images (640  $\times$  480) at four different poses.

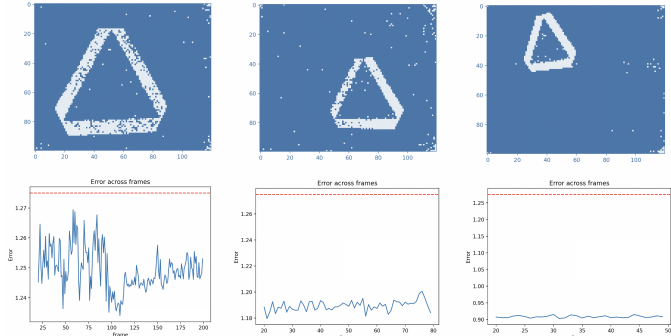


Fig. 17. Examples of noisy images and the noise value across multiple frames.

the target object, with pose space:

$$\Xi = [-0.2, 0.2] \times [0.33, 0.6] \times [1, 3.5] \times [0.01, 0.1]^3.$$

An encoder  $\mathcal{N}_D$  is implemented as a two-layer fully connected network with layer sizes 256–200–6 and sigmoid activations. It is trained with the Adam optimizer ( $\text{lr} = 10^{-4}$ , batch size 128) for 50 epochs using the Smooth L1 loss. To promote robustness, we include Lipschitz regularization ( $\lambda = 0.1$ ) and apply neuron clipping at 0.05. To evaluate the trained encoder, the pose space is discretized into a grid with step size  $\eta = 0.01$  in each dimension, yielding approximately 4.7 M data points. A total of 1 M random poses (unseen during training) were sampled for testing. The test error histogram of the 1 M random poses is shown in Fig. 18, where the encoder attains a mean error of 0.181 and a maximum error of 0.826, with 99.99% of samples below 0.65, closely matching the training performance. We then compute the certified error

TABLE IV. Certified maximum error bounds for each dimension of the pose estimate.

Dimension $i$	$\eta$	$L_{\Delta} L_D$	$\epsilon$	$e_D^i$
$x$	0.01	6.45	0.40	0.47
$y$	0.01	6.45	0.27	0.34
$z$	0.01	6.45	0.76	0.83
$\theta, \phi, \psi$	0.01	6.45	0.09	0.16

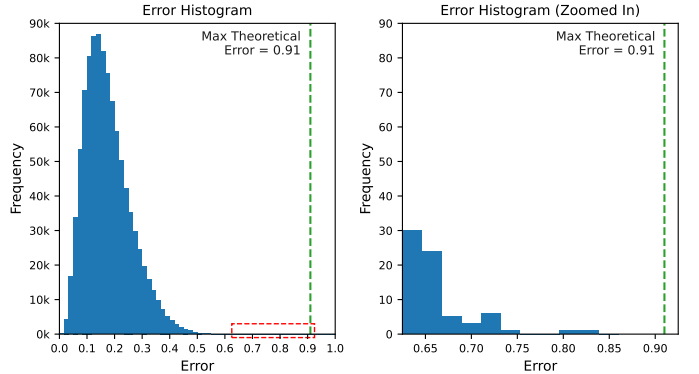


Fig. 18. Test error histogram for the encoder using 1 M unseen random poses.

bound for the encoder as follows:

$$\begin{aligned} e_D &\leq \eta (L_{\Delta} L_D + 1) + \epsilon \\ &= (0.01) (6.45 + 1) + 0.84 \approx 0.91. \end{aligned}$$

From the error histogram in Fig. 18, the maximum test error observed is 0.845, which is within the certified bound of 0.91, validating the theoretical bound provided by Theorem 1. The maximum theoretical error in each dimension is summarized in Table IV.

#### D. Experiment 3: Detection and Pose Estimation in Cluttered Environments

We now evaluate the performance of our detection and pose estimation pipeline in cluttered environments. The goal of this experiment is to assess the ability of our framework to accurately detect and estimate the pose of a runway in the presence of noise and other objects in the scene. The pose space of interest spans  $\xi_y \in [0.8 \text{ m}, 1.0 \text{ m}]$ ,  $\xi_z \in [1.6 \text{ m}, 1.8 \text{ m}]$ ,  $\xi_{\theta} \in [0.5, 0.7] \text{ rad}$ , with  $\xi_x = 0$  fixed. We partition this region into  $K = 27$  hypercubes with spacing  $\delta = 0.1$  and construct the certified object detector  $\mathcal{N}_{\Xi_i}$  and spatial filter

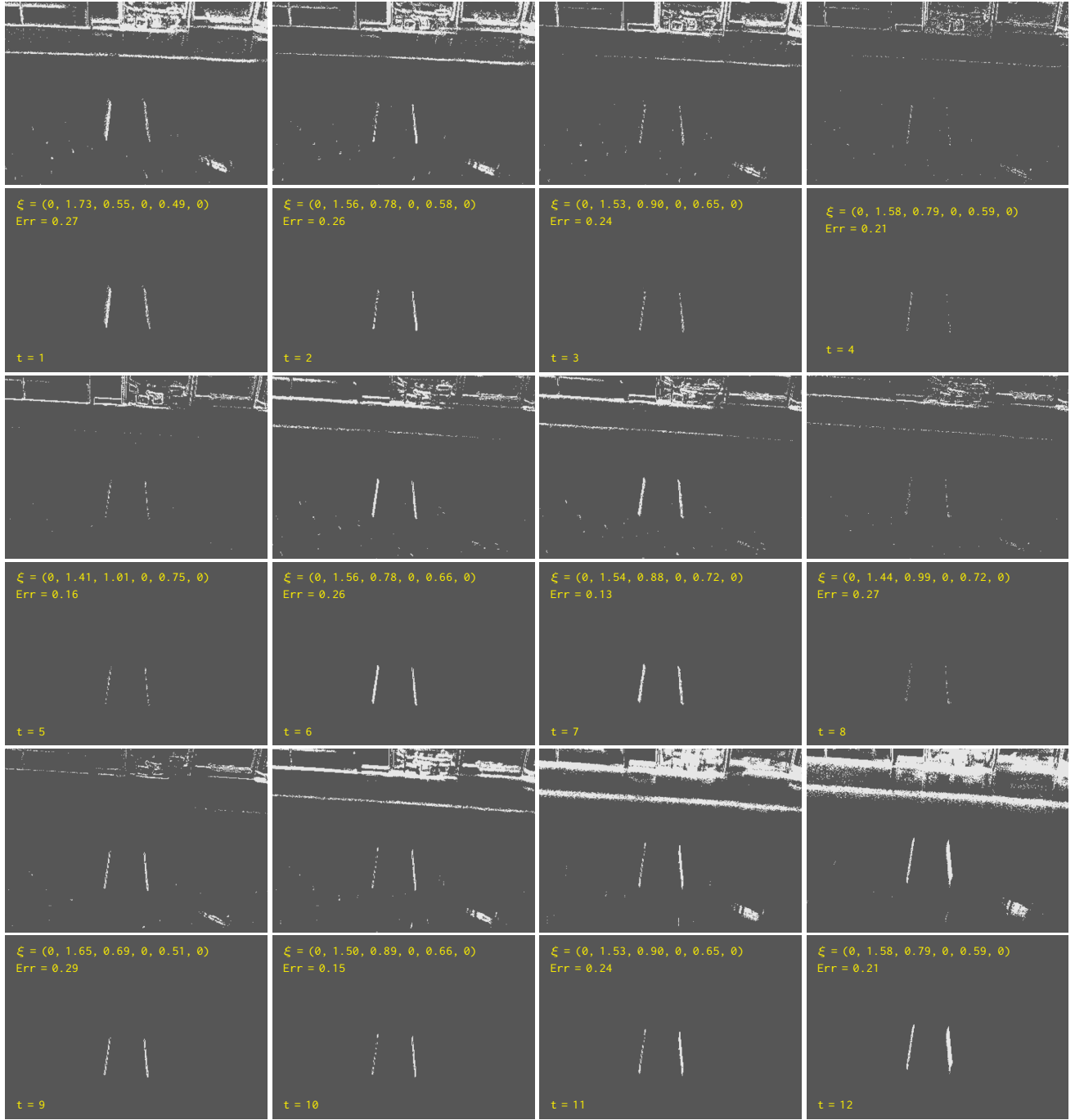


Fig. 19. Temporal sequence comparison between raw camera image  $I$  (top) and filtered output  $\tilde{I}$  (bottom) at five representative timestamps. Each filtered image displays the estimated pose  $\xi$  and the corresponding estimation error (Err). Both filtered outputs and pose estimates were obtained using the pose estimation pipeline described in Section VI. The results demonstrate successful detection, clutter removal, and accurate pose estimation within certified bounds.

$H_i$  for each cell  $i = 1, \dots, 27$ . A total of 1,320 frames were collected by the camera at 25 fps. Fig. 19 shows a sequence of 12 representative frames. For each, we display the raw cluttered image and the filtered image produced by the spatial filtering pipeline. The top-right corner of each frame shows the estimated pose  $(\xi_\theta, \xi_y, \xi_z)$  and the corresponding error with respect to the ground truth. The results show that the spatial filtering pipeline is able to effectively remove clutter from the images, allowing for accurate pose estimation of the runway.

## VIII. CONCLUSION

This paper introduces a framework for certified vision-based pose estimation that addresses the critical gap in providing provable guarantees for neural network-based perception systems in safety-critical applications. The main contributions include the design of GGMs that encode camera and target geometry through analytically-derived rather than learned parameters, enabling formal verification through reachability analysis. Additionally, we developed a decoder-encoder archi-

ture with grid-based sampling that provides deterministic error bounds on pose estimation, and a multi-stage perception pipeline that extends certified estimation to cluttered environments through spatial filtering and reachability-based object detection. Empirical evaluations using both synthetic images and real event-based camera data demonstrate that the framework achieves reliable pose estimation within certified bounds across diverse scenarios. These contributions establish the GGM-based framework as a viable approach for certifiable vision-based perception, offering significant improvements in formal guarantees, detection robustness, and applicability to real-world autonomous systems.

## REFERENCES

- [1] “Advisory circular 150/5340-30j: Design and installation details for airport visual aids,” Federal Aviation Administration, Tech. Rep., March 2023, u.S. Department of Transportation, Federal Aviation Administration. [Online]. Available: [https://www.faa.gov/documentLibrary/media/Advisory\\_Circular/150-5340-30J.pdf](https://www.faa.gov/documentLibrary/media/Advisory_Circular/150-5340-30J.pdf)
- [2] “Advisory circular 150/5340-30m: Standards for airport markings,” Federal Aviation Administration, Tech. Rep., December 2020, u.S. Department of Transportation, Federal Aviation Administration. [Online]. Available: [https://www.faa.gov/documentLibrary/media/Advisory\\_Circular/150-5340-1M-Chg-1-Airport-Markings.pdf](https://www.faa.gov/documentLibrary/media/Advisory_Circular/150-5340-1M-Chg-1-Airport-Markings.pdf)
- [3] X. Huang, M. Kwiatkowska, S. Wang, and M. Wu, “Safety verification of deep neural networks,” in *Computer Aided Verification: 29th International Conference, CAV 2017, Heidelberg, Germany, July 24–28, 2017, Proceedings, Part I 30*. Springer, 2017, pp. 3–29.
- [4] H.-D. Tran, S. Bak, W. Xiang, and T. T. Johnson, “Verification of deep convolutional neural networks using imagestars,” in *International conference on computer aided verification*. Springer, 2020, pp. 18–42.
- [5] H.-D. Tran, N. Pal, P. Musau, D. M. Lopez, N. Hamilton, X. Yang, S. Bak, and T. T. Johnson, “Robustness verification of semantic segmentation neural networks using relaxed reachability,” in *Computer Aided Verification: 33rd International Conference, CAV 2021, Virtual Event, July 20–23, 2021, Proceedings, Part I 33*. Springer, 2021, pp. 263–286.
- [6] M. Ostrovsky, C. Barrett, and G. Katz, “An abstraction-refinement approach to verifying convolutional neural networks,” in *International Symposium on Automated Technology for Verification and Analysis*. Springer, 2022, pp. 391–396.
- [7] H. Khedr, J. Ferlez, and Y. Shoukry, “Peregrinn: Penalized-relaxation greedy neural network verifier,” in *Computer Aided Verification: 33rd International Conference, CAV 2021, Virtual Event, July 20–23, 2021, Proceedings, Part I 33*. Springer, 2021, pp. 287–300.
- [8] S. M. Katz, A. L. Corso, C. A. Strong, and M. J. Kochenderfer, “Verification of image-based neural network controllers using generative models,” *Journal of Aerospace Information Systems*, vol. 19, no. 9, pp. 574–584, 2022.
- [9] F. Cai, C. Fan, and S. Bak, “Scalable surrogate verification of image-based neural network control systems using composition and unrolling,” in *Proceedings of the AAAI Conference on Artificial Intelligence*, vol. 39, no. 1, 2025, pp. 21–30.
- [10] Y. Geng, Z. Zhou, Z. Zhang, S. Pan, H.-D. Tran, and I. Ruchkin, “Deterministic world models for verification of closed-loop vision-based systems,” *arXiv preprint arXiv:2512.08991*, 2025.
- [11] U. Santa Cruz and Y. Shoukry, “Nnlander-verif: A neural network formal verification framework for vision-based autonomous aircraft landing,” in *NASA Formal Methods Symposium*. Springer, 2022, pp. 213–230.
- [12] P. Habeeb, N. Deka, D. D’Souza, K. Lodaya, and P. Prabhakar, “Verification of camera-based autonomous systems,” *IEEE Transactions on Computer-Aided Design of Integrated Circuits and Systems*, vol. 42, no. 10, pp. 3450–3463, 2023.
- [13] U. Santa Cruz and Y. Shoukry, “Certified vision-based state estimation for autonomous landing systems using reachability analysis,” in *2023 62nd IEEE Conference on Decision and Control (CDC)*. IEEE, 2023, pp. 6052–6057.
- [14] P. Habeeb, D. D’Souza, K. Lodaya, and P. Prabhakar, “Interval image abstraction for verification of camera-based autonomous systems,” *IEEE Transactions on Computer-Aided Design of Integrated Circuits and Systems*, vol. 43, no. 11, pp. 4310–4321, 2024.
- [15] S. Mitra, C. Păsăreanu, P. Prabhakar, S. A. Seshia, R. Mangal, Y. Li, C. Watson, D. Gopinath, and H. Yu, “Formal verification techniques for vision-based autonomous systems—a survey,” in *Principles of Verification: Cycling the Probabilistic Landscape: Essays Dedicated to Joost-Pieter Katoen on the Occasion of His 60th Birthday, Part III*. Springer, 2024, pp. 89–108.
- [16] C. S. Păsăreanu, R. Mangal, D. Gopinath, S. Getir Yaman, C. Irimie, R. Calinescu, and H. Yu, “Closed-loop analysis of vision-based autonomous systems: A case study,” in *International Conference on Computer Aided Verification*. Springer, 2023, pp. 289–303.
- [17] Y. Li, B. C. Yang, Y. Jia, D. Zhuang, and S. Mitra, “Refining perception contracts: Case studies in vision-based safe auto-landing,” *arXiv preprint arXiv:2311.08652*, 2023.
- [18] D. Sun, B. C. Yang, and S. Mitra, “Learning-based inverse perception contracts and applications,” in *2024 IEEE International Conference on Robotics and Automation (ICRA)*. IEEE, 2024, pp. 11612–11618.
- [19] S. Yang, G. J. Pappas, R. Mangharam, and L. Lindemann, “Safe perception-based control under stochastic sensor uncertainty using conformal prediction,” in *2023 62nd IEEE Conference on Decision and Control (CDC)*. IEEE, 2023, pp. 6072–6078.
- [20] C. Hsieh, Y. Li, D. Sun, K. Joshi, S. Misailovic, and S. Mitra, “Verifying controllers with vision-based perception using safe approximate abstractions,” *IEEE Transactions on Computer-Aided Design of Integrated Circuits and Systems*, vol. 41, no. 11, pp. 4205–4216, 2022.
- [21] S. Ghosh, Y. V. Pant, H. Ravanbakhsh, and S. A. Seshia, “Counterexample-guided synthesis of perception models and control,” in *2021 American Control Conference (ACC)*. IEEE, 2021, pp. 3447–3454.
- [22] D. J. Fremont, J. Chiu, D. D. Margineantu, D. Osipovych, and S. A. Seshia, “Formal analysis and redesign of a neural network-based aircraft taxiing system with verifi,” in *International Conference on Computer Aided Verification*. Springer, 2020, pp. 122–134.
- [23] M. Abraham, A. Mayne, T. Perez, I. R. De Oliveira, H. Yu, C. Hsieh, Y. Li, D. Sun, and S. Mitra, “Industry-track: Challenges in rebooting autonomy with deep learned perception,” in *2022 International Conference on Embedded Software (EMSOFT)*. IEEE, 2022, pp. 17–20.
- [24] S. Dean, A. Taylor, R. Cosner, B. Recht, and A. Ames, “Guaranteeing safety of learned perception modules via measurement-robust control barrier functions,” in *Conference on Robot Learning*. PMLR, 2021, pp. 654–670.
- [25] C. Dawson, B. Lowenkamp, D. Goff, and C. Fan, “Learning safe, generalizable perception-based hybrid control with certificates,” *IEEE Robotics and Automation Letters*, vol. 7, no. 2, pp. 1904–1911, 2022.
- [26] M. Tong, C. Dawson, and C. Fan, “Enforcing safety for vision-based controllers via control barrier functions and neural radiance fields,” *arXiv preprint arXiv:2209.12266*, 2022.
- [27] C. Hsieh, Y. Koh, Y. Li, and S. Mitra, “Assuring safety of vision-based swarm formation control,” in *2024 American Control Conference (ACC)*. IEEE, 2024, pp. 3215–3222.
- [28] M. Gehrig and D. Scaramuzza, “Recurrent vision transformers for object detection with event cameras,” in *Proceedings of the IEEE/CVF Conference on Computer Vision and Pattern Recognition*, 2023, pp. 13884–13893.
- [29] R. Hartley and A. Zisserman, *Multiple view geometry in computer vision*. Cambridge university press, 2003.
- [30] J. Ferlez and Y. Shoukry, “Bounding the complexity of formally verifying neural networks: A geometric approach,” in *2021 60th IEEE Conference on Decision and Control (CDC)*. IEEE, 2021, pp. 5104–5109.
- [31] G. Katz, C. Barrett, D. L. Dill, K. Julian, and M. J. Kochenderfer, “Reluplex: An efficient smt solver for verifying deep neural networks,” in *International conference on computer aided verification*. Springer, 2017, pp. 97–117.
- [32] W. Fatnassi, H. Khedr, V. Yamamoto, and Y. Shoukry, “Bern-nn: Tight bound propagation for neural networks using bernstein polynomial interval arithmetic,” in *Proceedings of the 26th ACM International Conference on Hybrid Systems: Computation and Control*, 2023, pp. 1–11.
- [33] W. Fatnassi, A. Feeney, V. Yamamoto, A. Chandramowliswaran, and Y. Shoukry, “Bern-nn-ibf: Enhancing neural network bound propagation through implicit bernstein form and optimized tensor operations,” *IEEE Transactions on Computer-Aided Design of Integrated Circuits and Systems*, vol. 43, no. 11, pp. 4334–4345, 2024.
- [34] K. Xu, Z. Shi, H. Zhang, Y. Wang, K.-W. Chang, M. Huang, B. Kailkhura, X. Lin, and C.-J. Hsieh, “Automatic perturbation analysis for scalable certified robustness and beyond,” *Advances in Neural Information Processing Systems*, vol. 33, 2020.